JOURNAL OF GEOPHYSICAL RESEARCH, VOL. 113, C05017, doi:10.1029/2007JC004372, 2008

Mixed layer analysis of a mesoscale eddy in the Antarctic Polar Front Zone

Boris Cisewski,[1,2] Volker H. Strass,[1] Martin Losch,[1] and Hartmut Prandke[3]

Received 6 June 2007; revised 1 February 2008; accepted 28 February 2008; published 13 May 2008.

[1] Microstructure, acoustic Doppler current profiler, and conductivity-temperature-depth (CTD) profiles were taken in a mesoscale eddy in the Antarctic Polar Front Zone at about 2°15′E, 49°15′S during the R/V *Polarstern* cruise ANT XXI/3 within the scope of the European Iron Fertilization Experiment in January–March 2004. The mixed layer depth (MLD), calculated from the composite of CTD- and microstructure sonde (MSS)-derived data, was 97.6 ± 20.6 m. No significant correlation between the wind work (E_{10}) and the MLD (r = 0.02 to 0.22) was found. However, the analysis revealed a negative correlation between the surface buoyancy flux (B) and the MLD 1/2 d later. Two approaches were used to estimate the actively mixing layer depth (AMLD). First, the actively mixing layer was determined subjectively by analyzing the MSS-derived density, energy dissipation, and Thorpe scale profiles, and second, the mixed layer model embedded in a general circulation model was used. The overall mean of the determined depths of the actively mixing layer ($AMLD_{MSS}$ = 66.4 ± 28.8 m) agreed with the model-predicted boundary layer depths (BLD) (BLD_{KPP} = 69.1 ± 29.5 m), but the individual values sometimes were differing considerably. We deduced estimates of the vertical diffusivity (K_z) from the MSS-derived energy dissipation rates and Thorpe scales. Both methods showed that K_z decreased with depth from order of magnitude 10^{-1} m^2 s^{-1} in the actively mixed layer to order of 10^{-4} m^2 s^{-1} in the pycnocline.

Citation: Cisewski, B., V. H. Strass, M. Losch, and H. Prandke (2008), Mixed layer analysis of a mesoscale eddy in the Antarctic Polar Front Zone, *J. Geophys. Res.*, *113*, C05017, doi:10.1029/2007JC004372.

1. Introduction

[2] The oceanic mixed layer is defined as the quasi-homogeneous region of the upper ocean that directly interacts with the atmosphere. The mixed layer dynamics are primarily determined by the action of turbulent mixing of the water mass due to wind stress and convection driven by buoyancy fluxes at the air-sea interface, which reveal variations on hourly through diurnal and seasonal to interannual timescales. Understanding of the processes by which the mixed layer properties vary is essential for quantitative diagnostics of the coupled ocean and atmosphere system and its effect on biogeochemical cycles and ecosystems. The interaction between the mixed layer and the underlying pycnocline determines the ventilation of the ocean interior [e.g., *Luyten et al.*, 1983; *Woods*, 1985], influences the large-scale circulation and also the mesoscale variability [*Strass et al.*, 1992], and may impact the atmosphere in remote regions where the flow returns to the mixed layer [*Blanke et al.*, 2002]. A paradigm in marine biology that has existed since the pioneering work of *Sverdrup* [1953] is that the vernal shallowing of the mixed layer sets the conditions for the phytoplankton spring bloom. Also, ice edge blooms appear in fact to be triggered by the meltwater-mediated shallowing of the mixed layer [*Strass and Nöthig*, 1996]. Deep mixed layers have been put forward to explain the rather low productivity of whole ocean regions such as the Antarctic Circumpolar Current [*Tranter*, 1982]. Climatic differences of the Southern Ocean mixed layer depth on geological timescales and their impact on the biological pump of carbon that is associated with phytoplankton primary production have even been proposed as an explanation of glacial-interglacial variations of the atmospheric carbon dioxide concentration [*Francois et al.*, 1997]. Detailed observations of mixed layer structures and processes are, however, particularly rare in the open Southern Ocean in particular.

[3] Various definitions of the mixed layer depth (MLD) have been published. Basically, two types of criteria are mostly in use: difference criterions and gradient criterions, summarized and discussed by *Lukas and Lindstrom* [1991], *Brainerd and Gregg* [1995], *Kara et al.* [2000], and *Zawada et al.* [2005]. The first class is based on specifying a difference in temperature or density from the surface value, whereas the second class is based on specifying a gradient in temperature or density. The different estimates of MLD can deviate by 1 order of magnitude depending on the chosen criterion [*Zawada et al.*, 2005]. In regions where

[1] Alfred Wegener Institut für Polar und Meeresforschung, Bremerhaven, Germany.
[2] Now at Institut für Umweltphysik, Abteilung Ozeanographie, Universität Bremen, Bremen, Germany.
[3] ISW-Wassermesstechnik, Petersdorf, Germany.

0148-0227/08/2007JC004372$09.00

both the daily and seasonal cycles of the forcing are mainly dominated by the heat flux, the temperature-based criteria are sufficient to predict the mixed layer depth. When the wind is constant over periods longer than 1 d, the mixed layer often shows a strong diurnal cycle with nighttime convection due to cooling driving active mixing from the surface to the seasonal pycnocline, while during daytime, a shallower restratification may result from radiative heating. However, precipitation and ice melt can lead to stratifying pools of fresh water, which demands a density-based criterion.

[4] *Kara et al.* [2000] compared different gradient and difference criteria for estimating the MLD and concluded that considerable differences in the MLD result. Therefore they introduced an optimal algorithm for isotherm layer depth and MLD calculation developed through subjective analysis of temperature and density profiles from the work by *Levitus et al.* [1994] and *Levitus and Boyer* [1994]. One problem of estimating MLD from the available global data sets is, however, the coarse vertical resolution [*Lorbacher et al.*, 2006] and the fact that data from a wider latitude/longitude grid cell are horizontally averaged. While the surface layer of the ocean exhibits in conceptual models a very simple structure, a well-mixed layer of variable depth at the sea surface, and a seasonal pycnocline connecting the mixed layer to the permanent pycnocline, several processes can alter this picture [*Moum and Smyth*, 2001]. In consequence, the surface layer can include strongly stratified layers, actively mixing layers, salinity barrier layers, fossil mixed layers, and inversions [*Sprintall and Roemmich*, 1999].

[5] In order to understand the diurnal cycle of heat storage within the surface mixed layer, *Brainerd and Gregg* [1995] proposed two concepts of mixed layers, differing in the timescale over which they are mixed. They distinguished between the mixed layer, representing the zone of relatively homogeneous water formed by the history of mixing, and the actively mixing layer (AML), the zone in which mixing is occurring. To identify the mixing layer, they analyzed profiles of the kinetic energy dissipation rate (ε) and the length scale of turbulent overturns (L_T) and compared them to the signals both in temperature and density. The authors showed that both difference and gradient criteria are capable of describing the mixed layer depth. However, neither definition gave mixing layer depths that consistently matched the turbulence measurements. They concluded that overturning or so-called Thorpe scales [*Thorpe*, 1977] are the most reliable measure of mixing layer depths.

[6] For both the ocean-atmosphere coupling and the primary production by phytoplankton, it makes a difference if the surface layer is turbulent and actively mixing or merely homogenized by previous mixing events. *Sverdrup* [1953], in his fundamental theory about the development of phytoplankton blooms, defined as the criterion a critical depth, which is given by that depth at which, starting with integration at the surface, the vertically integrated photosynthetic production of phytoplankton cells that are assumed to be rapidly vertically mixed equals the integrated phytoplankton losses. Thus Sverdrup considered phytoplankton primary production in the actively mixing layer depth (AMLD). Despite that, in most applications of Sverdrup's theory to explain observed phytoplankton blooms, the MLD is taken as the control variable of light limitation instead of the AMLD.

[7] Here we present the results of a case study performed to determine the differences of the depths of the AML and the mixed layer (ML). While our results can contribute to a more accurate assessment of the role of light limitation for open ocean primary production and to a better understanding of variations of food supply for the higher trophic levels worldwide, they are of particular interest for the Southern Ocean. In our study, we also derive estimates of vertical diffusivity within and below the mixed layer. Estimates of vertical diffusivity are needed for calculating, for instance, the exchange of total carbon across the mixed layer base and the replenishment of phytoplankton nutrients in the mixed layer from below.

[8] Our study was conducted in the vicinity of the Antarctic Polar Front (APF) during the European Iron Fertilization Experiment (EIFEX) (*Polarstern* Cruise ANT XXI/3) [*Smetacek*, 2005]. The experiment was carried out in Lagrangian manner within a cyclonic eddy of a diameter of nearly 100 km. The eddy, centered at about (2°15′E, 49°15′S), was obviously shed from the APF by detachment of a northward protruding meander (Figure 1a). Since the experiment has been conducted within one particular hydrographic feature, it is ideally suited for the study of temporal changes, as advective effects are kept low.

[9] The paper is organized as follows. Section 2 describes the instrumentation and the data set. In section 3, we present the various methods for investigating the mixing regime within the upper 400 m from the different types of data. In order to analyze the response of the mixed layer to the forcing, we distinguish in section 4 between horizontal eddy effects and atmospheric fluxes. In section 5, we present conclusions.

2. Instrumentation

2.1. Conductivity-Temperature-Depth (CTD) Profiler

[10] During the experiment, 251 casts were taken between 11 February and 20 March 2004 from R/V *Polarstern* with a Sea-Bird 911plus CTD sonde, mostly to a pressure of 500 dbar; however, 18 casts penetrated deeper than 3000 dbar. From 14 to 22 February 2004, a fine-scale quasi-synoptic survey, consisting of eight parallel sections 20 km apart, was made to cover the meander structure and an embedded cyclonic eddy in an area of roughly 160 km west-east by 250 km south–north (Figure 1a) within the Antarctic Polar Front Zone. Water samples were collected with a Sea-Bird Carousel sampler with 24 12 L bottles. For in situ calibration, temperatures were measured with a digital reversing thermometer, Sea-Bird SBE35, and salinity samples were analyzed with a Guildline Autosal 8400A salinometer onboard. The temperature sensor was calibrated at the manufacturer a few months prior to the cruise and afterward to an accuracy better than 0.0001°C. Salinity derived from the CTD measurements was calibrated to a final accuracy of better than 0.002 by comparison to the salinity samples.

2.2. Acoustic Doppler Current Profiler (ADCP)

[11] Current velocities were measured continuously using a hull-mounted 153.6 kHz RDI narrowband ADCP. *U*

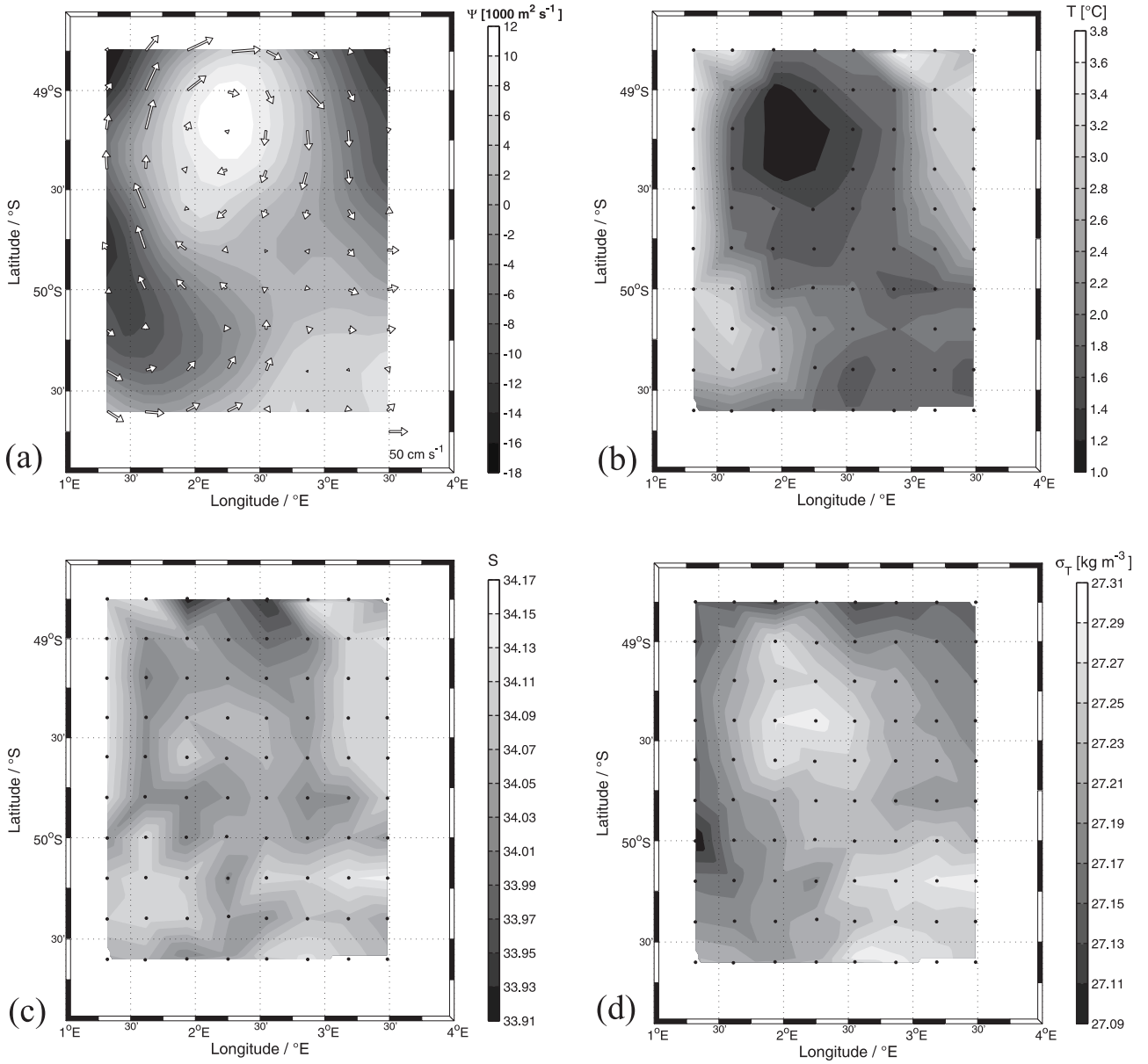

Figure 1. (a) ADCP velocity vectors averaged between 150 and 200 m and 10 km along track and stream function Ψ (1000 m^2 s^{-1}) showing a closed cyclonic circulation centered at 2°15′E and 49°15′S, which extends over roughly 100 to 150 km diameter. Horizontal distribution of (b) temperature, (c) salinity, and (d) density at the 200 m depth level.

(eastward) and V (northward) velocity components were averaged in 2 min ensembles in 4 m thick depth bins between 19 and 335 m depth. The transducers were located 11 m below the waterline. The reference layer was set to bins 6 to 15, avoiding near-surface effects and biases near bin 1. Heading, roll, and pitch data from the ship's gyro platforms were used to convert the ADCP velocities into Earth coordinates. The ship's velocity was calculated from position fixes obtained by the GPS or Differential Global Positioning System, if available. Accuracy of the ADCP velocities mainly depends on the quality of the position fixes and the ship's heading data. Further errors stem from a misalignment of the transducer with the ship's centerline. To reduce these errors, standard water track calibration methods were applied to provide a velocity scale factor and a constant angular offset between the transducer and the length axis of the ship. The further ADCP processing was done by using the CODAS3 software package developed by *Firing* [1991].

2.3. Microstructure Profiler

[12] Measurements of turbulence parameters were made with a microstructure profiler type MSS90. The general behavior of the microstructure sonde (MSS) profiler, produced by Sea & Sun Technology GmbH in cooperation with ISW Wassermesstechnik Dr. Hartmut Prandke, is described in detail by *Prandke et al.* [2000]. The MSS profiler is a loosely tethered, free-sinking instrument for simultaneous microstructure and precision measurements of physical parameters in marine and limnic waters. It was designed

for vertical profiling within the upper 400 m. The data were transmitted via electrical cable to an onboard unit and further to a data acquisition PC. The sinking rate of the profiler was adjusted to approximately 0.7 m s^{-1}, which was a good compromise between dissipation rate detection level and profiler handling. Because of ship drift, pycnoclines, and shear layers, the real sinking velocity varied between 0.6 and 0.8 m s^{-1}. The MSS profiler was equipped with two microstructure shear sensors, a microstructure temperature sensor, and standard CTD sensors for precision measurements. Sensor calibrations were carried out before and after the cruise. The drift of the CTD sensors are negligible. All sensors were mounted at the measuring head of the profiler. The microstructure sensors were placed at the tip of a slim shaft, about 150 mm in front of the CTD sensors. The sampling rate for all sensors was 1024 samples s^{-1}, and the resolution was 16 bit. Between 11 February and 20 March 2004, 167 MSS casts were performed at 33 hydrographic stations.

2.4. Meteorological Observations

[13] Standard meteorological parameters at or near the sea surface were continuously recorded by a multitude of measuring devices installed on R/V *Polarstern* [*König-Langlo et al.*, 2006] and archived by the ship's data acquisition system. Time series of the wind speed, air temperature, relative humidity, sea surface temperature, surface salinity, global radiation, and precipitation are used to investigate the meteorological forcing of the mixed layer. Wind speeds are derived from anemometer measurements made at 39 m height above the sea surface and corrected to a height of 10 m, accounting for atmospheric stability using the Coupled Ocean-Atmosphere Response Experiment (TOGA/WCRP) COARE 3.0 algorithms [*Fairall et al.*, 2003]. Air temperature and relative humidity are measured at a height of 29 m above the waterline. The sea surface temperature is measured at depths of 5 m and 11 m below sea level. Since the parameterization after the paper by *Large and Pond* [1981] does not take full stability into the account, we repeated the calculation with the more advanced COARE 3.0 algorithm. Comparing both algorithms reveals that COARE predicts higher C_D values than *Large and Pond* [1981] for wind speeds >10 m s^{-1}. While the calculated wind speeds can differ considerably during periods of strong winds, the differences between the averaged wind speeds and derived wind energy fluxes are only slight.

3. Methods

3.1. Meteorological Conditions and Surface Fluxes

[14] Energy driving the turbulent mixing in the upper ocean is provided by the wind stress and the surface buoyancy flux. To analyze for the wind forcing on the mixed layer, we first calculated the energy flux from the wind to the ocean surface as $E_{10} = \tau U_{10}$, where τ is the wind stress and U_{10} is the wind speed at 10 m. Second, we calculated the three components of the net heat flux Q from the ocean as $Q = \mathrm{SE} + \mathrm{LE} + F$, where SE is the sensible heat flux, LE is the latent heat flux, and F is the net radiative flux at the surface. For our computations, a constant sea surface albedo of 0.06 is applied. Positive Q values correspond to a flux from the atmosphere to the ocean. From the contribution of the surface heat flux and the surface fresh water flux, we obtain the surface buoyancy flux, estimated after the paper by *Shay and Gregg* [1986] as

$$B = \frac{g}{\rho_w}\left[\frac{\alpha}{c_w}Q + \frac{\beta s}{L(1-s)}\mathrm{LE}\right], \tag{1}$$

where g is the acceleration due to gravity, α is the thermal expansion coefficient, β is the haline contraction coefficient, c_w is the specific heat of seawater, Q is the net heat flux into the ocean, s is salinity expressed as a concentration, L is the latent heat of evaporation, and LE represents the latent heat flux (see also Table 1). Negative fluxes represent a loss of buoyancy from the ocean. Since the ship's rain gauge failed in the middle of the cruise, the surface freshwater flux was estimated by using the surface salinities measured by the thermosalinograph (H. Leach, personal communication, 2007).

3.2. Estimation of Turbulent Quantities

[15] To investigate the vertical mixing regime of the upper 400 m of the study area and its temporal development, we derived Thorpe scales (L_T), energy dissipation rates (ε), and the resulting vertical eddy diffusivities K_T and K_ε from 167 MSS casts. To cope with the problem of intermittence of turbulence, usually 4–6 MSS casts were conducted at each station position and then averaged.

[16] *Thorpe*'s [1977] method is used for estimating the vertical length scales of turbulent overturns, which represent patches of actively mixing fluid. The method consists of reordering an observed potential density profile or temperature profile, which may contain inversions, into a stable monotonous profile, which contains no inversions. The Thorpe displacements (d) are then given by the vertical shifts of data points needed to achieve static stability. The Thorpe scale (L_T) is given by the root mean square of an ensemble of Thorpe displacements,

$$L_T = \overline{(d^2)}^{1/2}. \tag{2}$$

[17] It provides a statistical measure of the vertical size of the overturning eddies in that profile segment [*Dillon*, 1982]. We calculate the Thorpe scales from the density profiles provided by the MSS profiler. Sensor response time, corrected temperature, and conductivity measurements were used to compute salinity and density in depth intervals of 0.1 m for the MSS data. The Thorpe scale is a very sensitive parameter to indicate the depth of the active mixed layer. This is due to the fact that Thorpe displacements are generated by turbulent dissipation and also by vertical convection. Under conditions of very weak stratification and low net heat flux at the sea surface (as we had during EIFEX), both processes must be taken into account. Vertical convection is an effective process in near-surface mixing. Another scaling technique, such as the Ozmidov scale [*Ozmidov*, 1965], reflects only one process (turbulent flows under stable stratification). However, the determination of the Thorpe scale under conditions of weak stratification is also difficult and requires density profiles with very low noise level. Since the MSS has a sampling rate of 1024 s^{-1}, our 0.1 m depth bins for Thorpe displacement computation

Table 1. List of Symbols

Symbol	Value	Unit	Definition
B		W kg^{-1}	surface buoyancy flux
B_S		W kg^{-1}	haline buoyancy flux
B_T		W kg^{-1}	thermal buoyancy flux
c_w	4.1×10^3	J kg^{-1} K^{-1}	specific heat of seawater
d		m	Thorpe displacement
E_{10}		W m^{-2}	wind work at 10 m height
F		W m^{-2}	net radiative flux at the surface
g		m s^{-2}	acceleration due to gravity
K_z		m^2 s^{-1}	vertical eddy diffusivity
L	2.3×10^3	W m^{-2}	latent heat of evaporation of seawater
LE		W m^{-2}	latent heat flux
L_T		m	Thorpe Scale
N		s^{-1}	buoyancy frequency
Q		W m^{-2}	net surface heat flux
S		none	salinity
SE		W m^{-2}	sensible heat flux
T_a		K	air temperature
T_w		K	water temperature
U, V		m s^{-1}	water velocity components
u_{10}		m s^{-1}	wind speed at 10 m height
u_*		m s^{-1}	friction velocity
α		none	thermal expansion coefficient
β		none	haline contraction coefficient
γ	0.2	none	mixing efficiency
ε		W kg^{-1}	kinetic energy dissipation rate
ν		m^2 s^{-1}	kinematic viscosity of seawater
ρ_a	1.25	kg m^{-3}	air density
ρ_w	1028	kg m^{-3}	water density
$\Delta\sigma_T$	0.02	kg m^{-3}	density difference criterion
τ		kg m^{-1} s^{-2}	wind stress
KPP notation			
f		s^{-1}	Coriolis parameter
h		m	boundary layer depth
h_E	0.7	m	Ekman depth
L_{MO}	1	m	Monin-Obukhov length
K_x		m^2 s^{-1}	vertical diffusion coefficient
Ri_b		none	bulk Richardson number
Ri_c	0.3	none	critical Richardson number
w_x		m s^{-1}	turbulent velocity scale
γ_x		K m^{-1}	nonlocal transport term
σ		none	vertical coordinate

are based on average values of (response time-corrected) temperature and conductivity of approximately 130 individual measurements (at a sinking rate of approximately 0.7 m s^{-1}). Thus small density instabilities can be detected safely. Furthermore, we applied spike removal procedures after the response time correction of the temperature and the computation of salinity. We performed Thorpe displacement computations with density profiles cut after the third and fourth decimal (in order to avoid an overestimation of Thorpe displacements because of noise). The computed scales differed only slightly. This indicates that the Thorpe scale computation is a robust method that can be applied not only in stably stratified depth ranges (pycnocline) but also in weakly stratified water. The dissipation rate ε has been calculated from the shear values using the equation for isotropic turbulence, $\varepsilon = 7.5\nu\ \overline{(du/dz)}^2$, where ν is the kinematic viscosity of water and du/dz is the velocity shear. Since the kinematic viscosity is weakly dependent on salinity and pressure but strongly dependent on temperature [*Siedler and Peters*, 1986], we used the following polynom, where $\nu = 1.792747 - 0.05126103T + 0.0005918645T^2$ (ν in 10^{-6} m^2 s^{-1}, T in °C) and ranges within $1.56–1.74 \times 10^{-6}$ m^2 s^{-1} for the recorded range of temperature, 0.97–4.88°C.

[18] The velocity shear is derived from the measurements by integrating the power spectrum in the wave number range from 2 to 30 cpm. The limitation of the high wave number cutoff to 30 cpm is due to the narrowband vibration peak in the wave number range above 30 cpm. The low wave number cutoff at 2 cpm is to eliminate contributions from low-frequency tumbler motions of the profiler. The calculated dissipation rates were corrected for the unresolved low wave number range (cutoff at 2 cpm) and high wave number range (cutoff at 30 cpm) of the spectrum. The correction coefficients were obtained from the universal turbulence spectrum. The variance was calculated in bins of 512 data records (corresponding to ~0.3 m depth intervals), with 256 records overlap of the depth bins. Finally, 1 dbar depth averages of the dissipation rates were calculated.

[19] The calculation of the dissipation rate was carried out for both shear sensors. Generally, the calculated dissipation rates showed a good agreement. A mean dissipation profile was calculated from both dissipation profiles. However, in many profiles, spikes occurred in one of the two dissipation profiles. We assume a hit of larger particles or zooplankton, which frequently occurred in the upper layer during the cruise, to be the reason for the isolated spikes. To eliminate an influence of these spikes in the mean dissipation profile calculated from the two sensors, the following procedure was applied: A mean dissipation value has been calculated if the values of one sensor did not exceed the other one by a factor of 5. If one sensor was larger by a factor of more than 5 in the respective depth interval, the smaller value was taken for the mean profile.

[20] Finally, all mean dissipation profiles have been inspected visually. In depth ranges of particularly high dissipation values, the vertical profiles of the shear data and the profiler acceleration were checked. If the high dissipation values were correlated with particularly high profiler vibration or extreme amplitudes in the shear signal (e.g., caused by large particles in the water), the calculated dissipation was substituted by interpolated values.

[21] Eddy diffusivities have been calculated for 1 dbar depth intervals from dissipation rates and Thorpe scales. The eddy diffusivity from dissipation was computed following *Osborn* [1980],

$$K_\varepsilon = \gamma\varepsilon/N^2, \tag{3}$$

where N is the buoyancy frequency, ε is the dissipation rate, and γ is the mixing efficiency. For the mixing efficiency γ, a constant value of 0.2 was used. From the squared Thorpe scale L_T^2, the buoyancy frequency N, and the mixing efficiency γ, the eddy diffusivity K_T was calculated as

$$K_T = \gamma L_T^2 N. \tag{4}$$

4. Results and Discussion

4.1. Hydrographic Structure and Circulation of the Eddy

[22] The fine-scale hydrographic survey covers a cyclonic eddy with a diameter of about 100 km, centered at 2°15′E,

49°15′S (Figures 1a, 1b, 1c, and 1d). The eddy was nearly stationary during the experiment, with small horizontal displacements of its center of rotation of less than 25 km [*Losch et al.*, 2006]. This eddy, shed by a northward protruding meander of the polar front, featured at its northwestern flank maximum velocities of about 1 m s^{-1} (Figures 1a and 2a). The boundary contours of this eddy are characterized by sharp gradients in temperature and density (Figures 1b and 1d). The temperature varies between a minimum core temperature (Figure 1b) of about 1°C at 200 m depth and higher values of above 3.5°C at the outer flanks of the meander. The cross-eddy transect reveals a fresher and warmer water mass at the northeastern boundary of the eddy (stations 55101 and 55202) (Figures 2b, 2c, and 2d). The water mass characteristics and vertical structure that typify the APF are described in more detail by *Strass et al.* [2002].

4.2. Meteorological Forcing and Surface Fluxes

[23] The eddy is located in a zonal band (45°S to 55°S) that is dominated by strong westerly winds, typical of the climate zone of the midlatitude westerlies. The synoptic weather systems in this storm track travel eastward around the Antarctic continent and are frequently intense because of the temperature contrast between ice and open ocean. *Wunsch* [1998] estimated that the Southern Ocean receives 70% of the work done by the wind on the ocean. Our wind records reveal two isolated peaks of wind forcing E_{10} in excess of 15 W m^{-2}, which occurred at year-day 50 and 54 and were accompanied by gale force winds of about 20 m s^{-1}. The mean value of u_{10} was approximately 11 m s^{-1}. The various terms in the meteorological forcing of the mixed layer are displayed in Figure 3. On average, the net heat flux was positive into the ocean (Figure 3d). The observed total heat flux at the surface was mainly dominated by the net radiative flux that ranged between −13 at night and 915 W m^{-2} during daytime, whereas the sensible and the latent heat fluxes ranged from −127 to 74 W m^{-2} and from −178 to 66 W m^{-2}, respectively (Figure 3c). Compared to the sensible and latent heat fluxes, the flux of kinetic energy from the wind field into the ocean, E_{10} (Figure 3a), was low, reaching a maximum of 23 W m^{-2}. These wind events result in latent heat losses of up to 128 W m^{-2} (compare Figures 3a and 3b at Julian day 51). The surface buoyancy flux (B) varied between -1.0×10^{-7} and 1.9×10^{-7} W kg^{-1} and revealed the typical daily cycle with buoyancy loss at night and buoyancy gain during the day. The salinity term usually makes a small contribution to the surface buoyancy flux. During the experiment, mean total buoyancy flux was 1.9×10^{-8} W kg^{-1}, and the mean salinity term was -2.8×10^{-9} W kg^{-1}, only 7% of the total.

4.3. Mixed Layer Depth

[24] For this study the MLD was defined, as in *Cisewski et al.* [2005], by the depth at which the calculated in situ density increased by $\Delta\sigma_T = 0.02$ compared to the surface value. To assess the suitability of this criterion and for the further discussion, we first apply it to a set of microstructure profiles, which give some insights into the processes involved. The variation of the mixed layer (Table 2) and the MSS-derived quantities are shown in Figure 4. A general upward increase of temperature in the upper 100 m is shown in Figure 4a. During the first 11 d of the experiment (stations 42407 to 50804), the MLD is found between 107 and 124 m. At station 51314, the MLD decreases to 51 m, followed by a period of increased values ranging between 82 and 127 m at stations 51419 to 55101 (day 60 to 69.7). While most of the measurements were made within the eddy, station 55201 was measured at its northeastern rim and shows the presence of warmer waters throughout the upper 400 m depth range.

[25] The buoyancy frequency squared, N^2, which gives a measure of the vertical stratification or the static stability of the water column, shows its maximum values of 2.5 to 4.5×10^{-4} s^{-2} in the depth range between 120 and 170 m just below the estimated MLD (Figure 4d). Thorpe scales (Figure 4e) in the mixed layer range between 2 and 21 m and thus indicate strong overturning at most stations. Just below the predicted mixed layer depth, the Thorpe scale decreases rapidly, indicating that the overturning is mainly driven by the surface forcing. The energy dissipation rate (Figure 4f) decreases in approximate exponential manner by up to 2 orders of magnitude (from 10^{-5} to 10^{-7} W kg^{-1}). At stations 51419, 54422, and 58013, the region of elevated ε coincides with the extent of overturning as indicated by the Thorpe scales. However, at the other stations, the region of high dissipation is restricted to the upper 20 to 70 m.

[26] To quantify the relationship between atmospheric forcing and the MLD, we calculated the correlation between the wind work E_{10} and MLD and between the surface buoyancy flux B and MLD at 200 stations (CTD and MSS) for varying time lags. Figure 5a illustrates the predicted mixed layer depths from both CTD and MSS profiles. The mean MLD calculated from the composite of CTD- and MSS-derived data is 97.6 ± 20.6 m. Because the 95% confidence for nonzero correlation is 0.138, the correlation between E_{10} and MLD is insignificant at most times. However, the analysis reveals a negative correlation between thermal buoyancy flux (B_T) and MLD. This correlation reflects the daily curve of the buoyancy flux. The highest correlation is −0.25 and −0.28 for time lags Δt = 13 h and Δt = 38 h. The correlation between the haline buoyancy flux (B_S) and MLD varies between −0.24 and −0.02. This result contradicts the findings of *Cisewski et al.* [2005] and *Lozovatsky et al.* [2005]. *Lozovatsky et al.* [2005] analyzed the dependence of the MLD on the sea surface fluxes on the basis of measurements taken along a cross-Atlantic section at 53°N. To quantify the relationship between atmospheric forcing on the MLD, they calculated the normalized cross-correlation function for varying time steps of 6 h. The highest correlation (0.71) between the MLD and the wind friction velocity u_* was found when u_* data preceded the mixed layer measurements by 12 h [*Lozovatsky et al.*, 2005]. The contradiction between those results may be caused by (1) the chosen correlation method and (2) the variability of the wind field. While our measurements were conducted within a stationary mesoscale eddy for the whole duration of the experiment, *Lozovatsky et al.* [2005] used the data of a cross-Atlantic transect at 53°N. On the basis of the assumption that the main cause of the mixed layer deepening and restratification is associated with synoptic scales of u_* and B driven by storm events, *Lozovatsky et al.* [2005] arranged their data as time series and not as space variables.

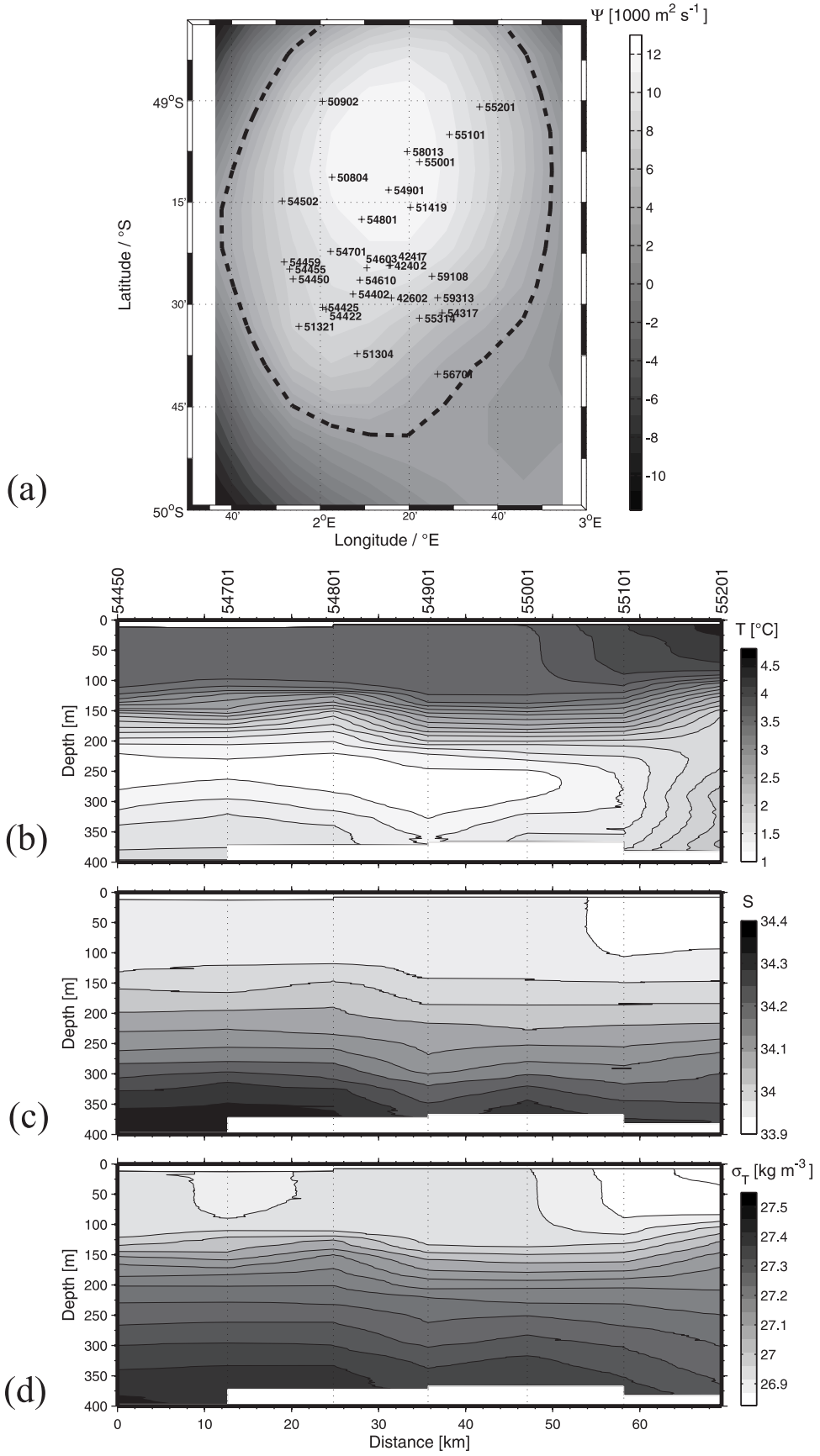

Figure 2. (a) Positions of all MSS in-eddy stations (black dashed line indicates the dimension of the eddy) and vertical distribution of (b) temperature T, (c) salinity S, and (d) density σ_T along cross-eddy section.

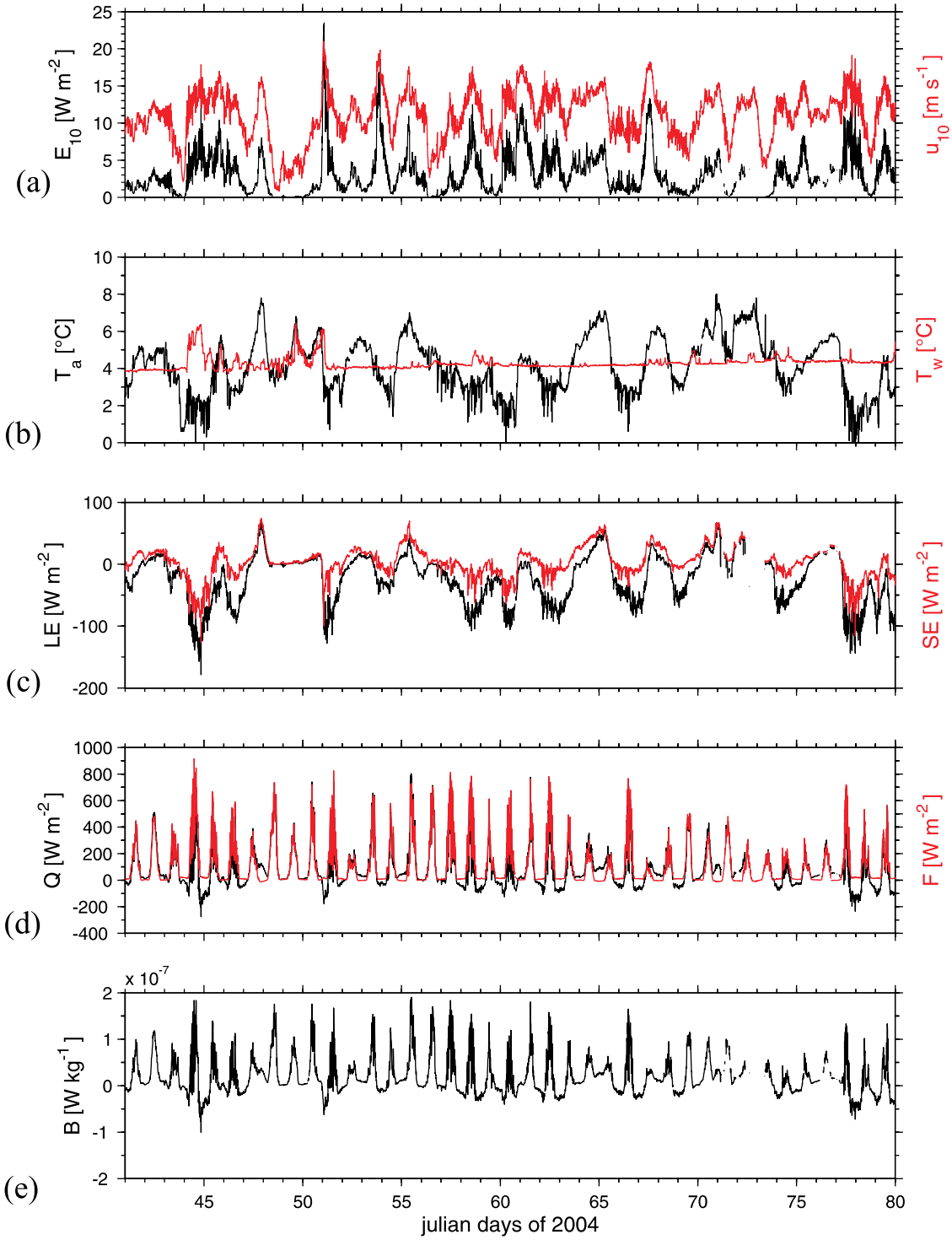

Figure 3. The 10 min averages of the meteorological data showing (a) E_{10}, the energy flux resulting from the wind stress (black) and wind speed (red); (b) air temperature T_a (black) and water temperature T_w (red); (c) latent heat and sensible fluxes LE (black) and SE (red); (d) total heat flux from atmosphere to ocean Q (black) and net radiative flux F (red); and (e) buoyancy flux B.

On the other hand, differences between the wind field of the northern Atlantic and the Southern Ocean might also account these differences. In a previous study, *Cisewski et al.* [2005] detected a significant correlation between MLD and the time-integrated wind energy flux converging to 0.83 after a time period of three inertial periods, which compares to 48 h, within a mesoscale eddy in the vicinity of the APF at 48°S.

4.4. Actively Mixing Layer Depth

[27] First, we determined the actively mixing layer from density, viscous dissipation, and Thorpe scale profiles. The

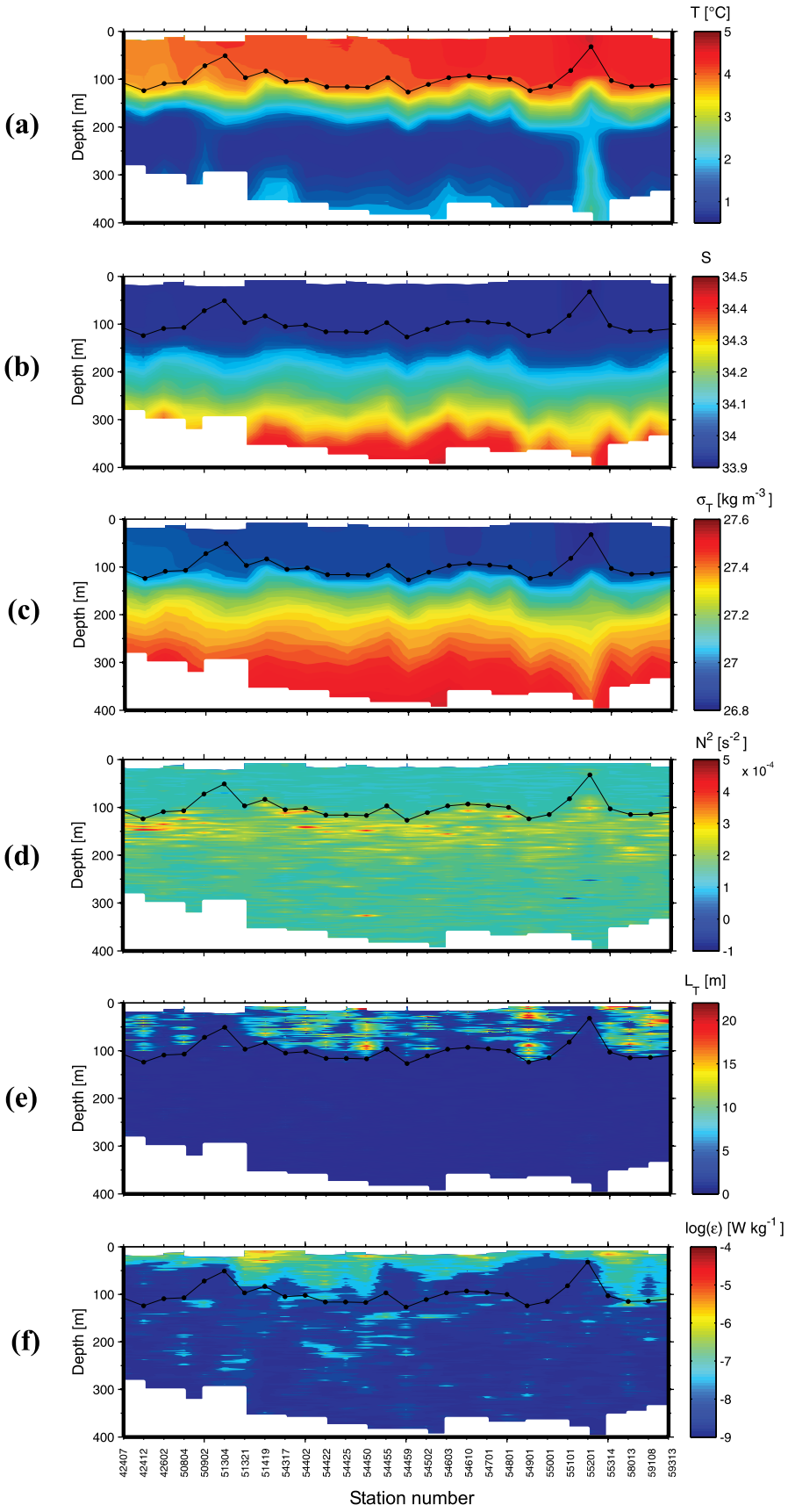

Figure 4. Vertical distribution of (a) temperature T, (b) salinity S, (c) density σ_T, (d) Brunt-Väisälä frequency squared N^2, (e) Thorpe scale L_T, and (f) kinetic energy dissipation rate ε measured at all in-eddy MSS stations (black curve indicates MLD).

Table 2. Station Mean Observations

Station	Latitude, South	Longitude, East	Start, decimal day	Actively Mixing Layer Depth, m	Mixed Layer Depth, m	E_{10}, W m^{-2}	Q, W m^{-2}	B, 10^{-7} W kg^{-1}
42407	49°24.11′	2°15.16′	41.86	38	108	1.48	21.96	0.05
42412	49°24.45′	2°15.54′	41.97	47	124	1.29	12.3	0.03
42602	49°29.06′	2°15.64′	43.56	52	109	0.44	266.6	0.59
50804	49°11.27′	2°02.48′	52.4	38	107	2.21	127.03	0.3
50902	49°00.14′	2°00.57′	53.3	42	72	1.48	99.79	0.24
51304	49°37.30′	2°08.30′	57.84	36	51	1.4	−28.47	−0.11
51321	49°34.10′	2°00.02′	58.38	57	97	5.77	247	0.49
51419	49°15.12′	2°20.90′	60.28	74	83	4.55	−24	−0.15
54317	49°31.25′	2°27.40′	63.51	91	105	2.41	371.32	0.81
54402	49°28.50′	2°07.35′	64.64	90	102	5.78	200.43	0.5
54422	49°30.70′	2°01.30′	65.56	97	116	0.62	166.08	0.41
54425	49°30.40′	2°01.00′	65.64	105	116	1.21	98.86	0.23
54450	49°26.36′	1°54.89′	66.34	105	117	1.03	181.96	0.37
54455	49°25.22′	1°53.71′	66.56	81	97	0.86	532.64	1.2
54459	49°23.70′	1°52.74′	66.71	58	127	1.84	63.49	0.08
54502	49°15.14′	1°51.98′	67.35	100	111	6.66	24.62	0.02
54603	49°24.33′	2°11.33′	68.59	57	97	0.74	191.12	0.45
54610	49°26.50′	2°08.90′	68.76	60	93	1.13	−18.87	−0.08
54701	49°22.04′	2°02.91′	69.23	77	96	0.51	−25.63	−0.11
54801	49°17.56′	2°09.35′	69.37	77	100	0.5	78.73	0.14
54901	49°13.26′	2°15.97′	69.47	109	124	0.28	444.71	1.02
55001	49°09.18′	2°22.53′	69.57	13	115	0.26	426.29	0.99
55101	49°04.91′	2°29.24′	69.67	24	82	0.75	211.83	0.51
55201	49°00.60′	2°35.80′	69.77	23	32	0.84	1.25	−0.01
55314	49°31.85′	2°23.71′	71.32	96	103	1.2	164.75	0.41
56701	49°40.43′	2°27.35′	72.74	45	85			
58013	49°07.76′	2°19.44′	75.47	38	115	5.2	132.88	0.3
59108	49°25.86′	2°25.72′	78.5	102	114	0.99	87.78	0.14
59313	49°28.90′	2°27.14′	79.29	93	110	3.81	3.03	−0.05

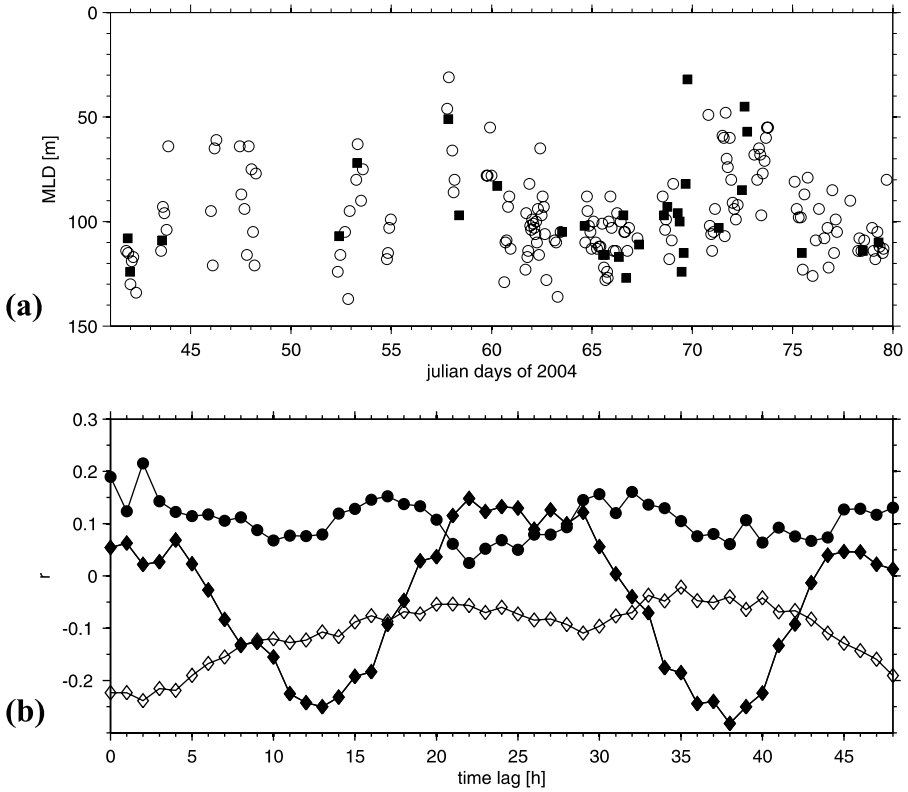

Figure 5. (a) MLD obtained from CTD (open circles) and MSS (solid squares) and (b) correlation coefficients between E_{10} and MLD (solid circles), correlation coefficients between B_T and MLD (solid diamonds), and correlation coefficients between B_S and MLD (open diamonds).

combination of MSS- and CTD-derived parameters enables a distinction between MLD and AMLD. How the MLD and AMLD (Table 2) are reflected by the various variables is depicted by three example profiles recorded between 8 and 10 March (Julian days 67 and 69). The results at the first station were obtained between 0730 and 0912 UT at Julian day 67. The density profile at this station (station 54502) (Figure 6a) reveals a quasi-homogeneous mixed layer with 100 m thickness. Wind forcing at that time was strong (u_{10} = 14.8 m s^{-1}), whereas the net surface heat flux Q was only 25 W m^{-2}. The high dissipation rate ($\varepsilon > 10^{-7}$ W kg^{-1}) in the uppermost 30 to 40 m also reflects the impact of direct wind stirring. The strong mixing is also revealed by large Thorpe scales between 3 and 19 m, which occur in the upper layer shallower than 99 m depth. This depth is not much different from the MLD estimated by the difference criterion as 111 m. The actively mixed layer with large Thorpe scales is separated from below by a sharp gradient, where the averaged Thorpe scales decrease from 6.32 to 1.02 m. In the same depth range, the dissipation rate decreases exponentially by 2 orders of magnitude from 10^{-6} to 10^{-8} W kg^{-1}.

[28] Station 54901 was conducted 48 h later (1037 and 1203 UT at Julian day 69). The density profile recorded at that station (Figure 6b) reveals a quasi-homogeneous mixed layer with 109 m thickness. The strong mixing is characterized by the highest Thorpe scales observed during the experiment, ranging between 1 and 21 m. The MLD predicted by the difference criterion to 124 m agrees well with the depth of the lower boundary of the layer marked by large Thorpe scales, estimated as 109 m. Although wind stirring was moderate (u_{10} = 6.0 m s^{-1}) and the net surface heat flux was high with a value of 445 W m^{-2} at the time of conducting the station, the mixed layer has deepened by 10 m during the last 48 h. The integrated buoyancy flux reveals a buoyancy loss of -1.7×10^{-8} W kg^{-1} for the last 12 h, which shows that the observed mixed layer deepening was mainly convectively driven during the previous night.

[29] Station 55101 was obtained only 3 h later (1526 and 1647 UT at Julian day 69), but closer to the northeastern boundary of the eddy. The density and temperature profile shows a layered structure in the upper 82 m of the water column, which reveals a new shallow mixed layer that overlies a uniformly mixed region of water mass formed during an earlier deep mixing event (Figure 6c). The vertical profile of the dissipation rate also reveals a layered structure. While increased winds (u_{10} = 8.2 m s^{-1}) cause high dissipation rates ($\varepsilon > 10^{-7}$ W kg^{-1}) within the upper 25 m of the water column, the dissipation rate decreases very rapidly within 25 to 30 m, which shows that the layer below was cut off from direct wind forcing. In this case, the lower boundary of the actively mixed layer can be defined as that depth where the dissipation rate decreases from 10^{-7} to $\sim 10^{-8}$ W kg^{-1} following *Lozovatsky et al.* [2006]. The lower boundary of the decoupled layer, which contains local overturns with Thorpe scales of up to 10 m, can be predicted well by the difference MLD criterion and was estimated as 82 m. We interpret the upper mixed layer as being formed in response to restratification due to an increased surface heat flux in the afternoon. Further hints for the stabilization arise from a rough calculation of the

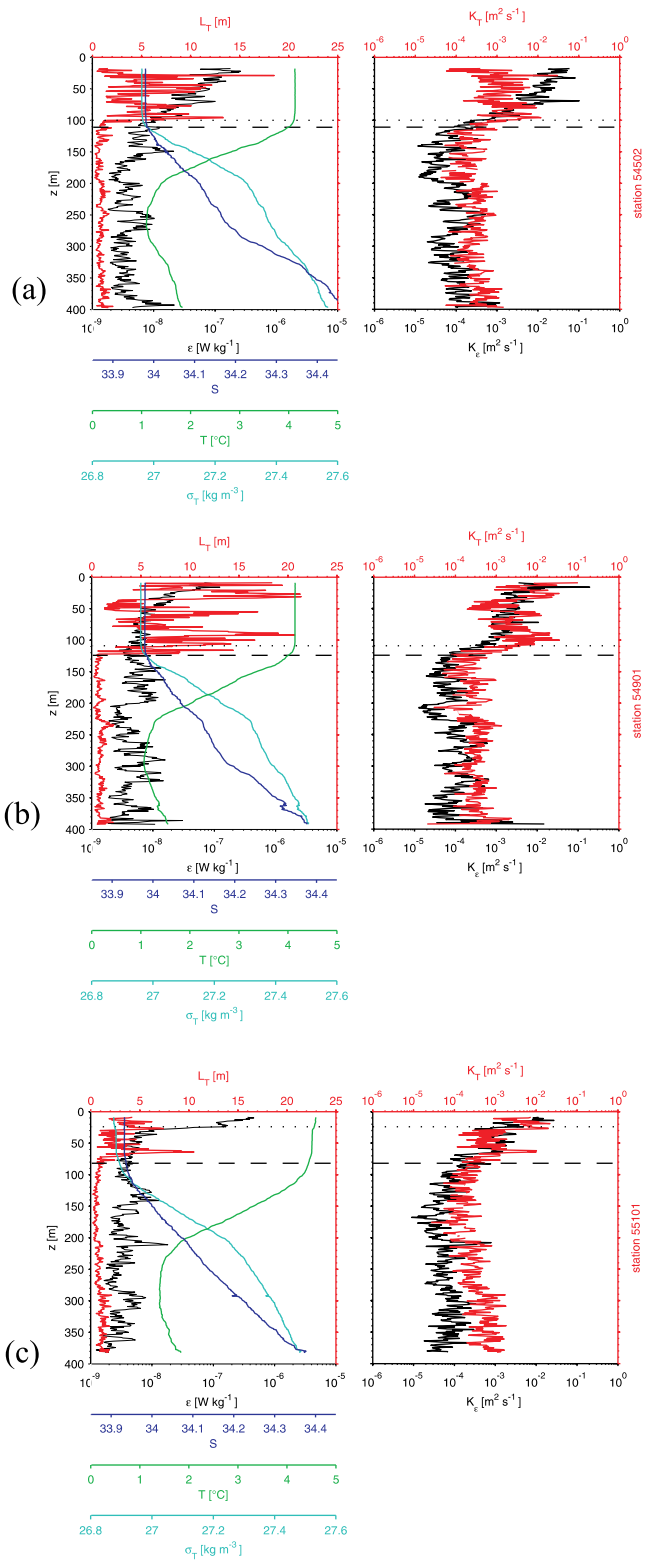

Figure 6. MSS profiles at stations (a) 54502, (b) 54901, and (c) 55101. Left panels show temperature T (green), salinity S (blue), density σ_T, (cyan), Thorpe scale L_T (red), kinetic energy dissipation rate ε (black), mixed layer depths (black dashed line), and actively mixing layer depths (black dotted line). Right panels show vertical distribution of K_ε (black) and K_T (red).

expected surface warming ΔT of the upper 20 m of the surface layer,

$$\Delta T = \frac{\sum_{t1}^{t2} \Delta t Q}{\Delta h \rho_w c_w}, \quad (5)$$

where Δt is the time interval in seconds, Q is the oceanic surface heat flux, and Δh is the thickness of the surface mixed layer (20 m). Using equation (5), the integrated surface heat flux measured between 0700 and 1640 UT results in a warming of about 0.1°C in the upper 20 m of the water column at station 55101, which is comparable with the observed warming of 0.062°C seen in the MSS temperature profile.

[30] As a second method to estimate the actively mixed layer depth, we used the mixed layer model of *Large et al.* [1994] as implemented in the Massachusetts Institute of Technology general circulation model (MITgcm) (MITgcm data are available at http://mitgcm.org/sealion/online_documents/manual.html). This mixed layer model is a first-order closure model with a nonlocal K-profile parameterization of *Troen and Mahrt* [1986].

[31] A nonlocal transport term γ_x is added to the diffusive down-gradient parameterization of turbulent flux of tracer x to yield $\overline{wx}$ (d) $= -K_x (\partial_z X - \gamma_x)$. The details of the present K-profile parameterization (KPP) model implementation follow *Large et al.* [1994] exactly. We only summarize main points here. The vertical diffusion coefficient K_x is expressed as the product of a depth-dependent turbulent velocity scale w_x and a nondimensional vertical shape function $G(\sigma)$ with dimensionless vertical coordinate $\sigma = d/h$. The extend of the ocean planetary boundary layer h depends on the surface forcing and on the oceanic buoyancy $B(z)$ and velocity (z) profiles. A bulk Richardson number relative to the surface is defined as

$$\mathrm{Ri}_b(d) = \frac{(B_r - B(d))d}{|\vec{V}_r - \vec{V}(d)|^2 + V_t^2(d)}, \quad (6)$$

and h is equated to the smallest value of the depth d at which this Richardson number equals a critical value Ri_c. The buoyancy B_r and velocity V_r are estimated as averages over a surface layer thickness. The destabilizing term that leads to the denominator of (6) includes the difference from the reference velocity and the turbulent velocity shear V_t/d. This term tends to increase entrainment fluxes at the base of the boundary layer in the case of large N (see *Large et al.* [1994] for details). With stable forcing ($B > 0$, $L = \mathrm{u}_*^3/(B\,f) > 0$), the boundary layer depth h is required to be less than both the Monin-Obukhov length (L_{MO}) and the Ekman depth. To compute the depth of the boundary layer, we use a critical bulk Richardson number of 0.3, the coefficient for Ekman depth as 0.7, and a coefficient for Monin-Obukhov depth as 1.0.

[32] We create a 3-D global state estimate from hydrography and velocity data by assimilating a general circulation model (MITgcm data are available at http://mitgcm.org/sealion/online_documents/manual.html) to the observations with the help of the adjoint method (M. Losch, manuscript in preparation, 2007). The state estimate is obtained for a 200 km × 150 km box with four open boundaries enclosing the experimental site. Lateral and surface boundary values are adjusted to fit the model to the observations. The boundary layer depth (BLD) and vertical diffusivity coefficients are extracted along the virtual cruise track in the simulated ocean.

[33] As effects from horizontal buoyancy gradients are neglected in KPP itself, these physical effects might constitute a possible explanation of the poor correlation between $\mathrm{AMLD_{MSS}}$ and $\mathrm{BLD_{KPP}}$. Therefore we analyzed whether lateral advection and related horizontal gradients affected the MLD and AMLD (Figures 7a, 7b, 7c, and 7d). As it is reasonable to assume that advective effects are strongest along the rim of the eddy, we use two quantities, for which the horizontal distribution pattern can be taken as a measure of distance from the eddy center. The illustrated horizontal distribution of the stream function (ψ) (Figure 2a) reveals a cyclonic eddy with an ellipsoidal shape. Since ψ decreases in a nearly linear manner from ~13 (1000 $\mathrm{m^2\ s^{-1}}$) at the center of the eddy to 3 (1000 $\mathrm{m^2\ s^{-1}}$) at the eddy rim, we interpolated the stream function for all MSS station positions, which were conducted within the eddy. The correlations between ψ and MLD and ψ and AMLD were 0.12 and −0.35, respectively. Because the 95% confidence level for nonzero correlation is 0.37, both correlations were insignificant.

[34] As a second quantity, we use the horizontal distribution of the minimum temperature, which is associated with the so-called Winter Water (WW). $T_{\mathrm{Min\ WW}}$ increases linearly from ~1.0°C at the eddy center to 1.5°C at the rim of the eddy. The correlation between $T_{\mathrm{Min\ WW}}$ and MLD reveals a significant negative correlation of −0.76, which implies that the mixed layer will get shallower with growing distance from the eddy center. Since only one of the four estimations reveals a significant correlation, we conclude that lateral advection and associated horizontal buoyancy gradients had a minor effect on the MLD/AMLD during the experiment.

[35] For the analysis, we diagnosed the $\mathrm{BLD_{KPP}}$ for all available MSS-derived AMLDs. Although the mean values ($\mathrm{AMLD_{MSS}}$ = 66.4 ± 28.8 m and $\mathrm{BLD_{KPP}}$ = 69.1 ± 29.5 m) are nearly the same, the individual values sometimes differ significantly, and the two variables show a correlation of not more than 0.48 (Figure 8). The largest deviation occurs at station 54901. The numerical model predicts a boundary layer depth of 25 m caused by restratification favorable conditions, which are characterized by a high net surface heat flux (Q) of about 445 $\mathrm{W\ m^{-2}}$ and a low wind energy flux (E_{10}) of about 0.28 $\mathrm{W\ m^{-2}}$ (Table 2). In contrast to this prediction, the MSS data show vigorous mixing down to 109 m. The difference between the estimated BLD and AMLD may be caused by several factors.

[36] Apart from the fact that the KPP boundary layer model is based on many parameterizations and as such is an approximation of reality, the results of KPP are largely determined by the surface boundary conditions. The atmospheric surface conditions for our specific 3-D model simulation are obtained from onboard meteorological observations and bulk formulae [*Large and Pond*, 1981; *Large and Pond*, 1982] and then adjusted by the steady state estimation procedure. The point measurements may not be representative for the entire model domain, and some

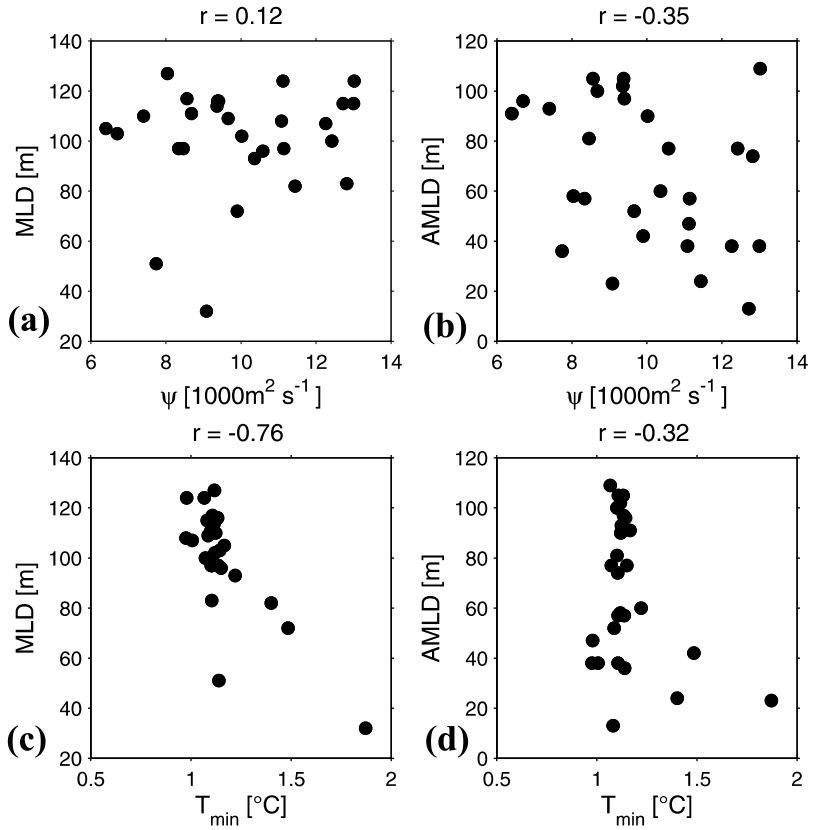

Figure 7. Correlation between (a) MLD and stream function Ψ, (b) AMLD and stream function Ψ, (c) MLD and $T_{\text{Min WW}}$, and (d) AMLD and $T_{\text{Min WW}}$.

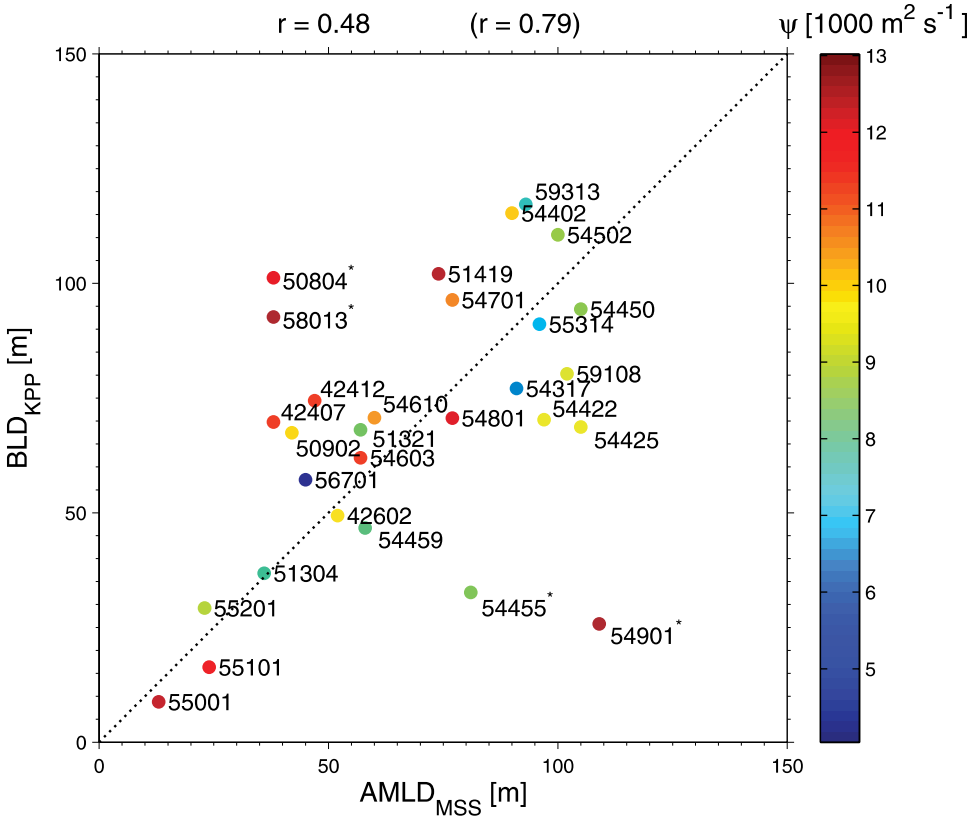

Figure 8. Correlation between BLD and AMLD. Color bar indicates relative position of the chosen MSS stations in terms of the stream function Ψ.

parameters were not always available; for example, the precipitation observations stop in the middle of the experiment because of instrument failure and had to be replaced by surface salinity observations, as mentioned in section 3.1. The bulk formulae may not be accurate for all meteorological situations encountered during the experiment. Furthermore, the model simulation cannot capture all details of the observations; biased model hydrography can effect stability computations and thus parameterized mixing. If we exclude those stations, which reveal the biggest deviations between $AMLD_{MSS}$ and BLD_{KPP} (indicated by asterisks in Figure 8), the correlation is about 0.79.

4.5. Vertical Diffusivities

[37] On the basis of three different approaches, station averages were computed for the vertical eddy diffusivity (K_z). For each station, average values of K_T and K_ε within the actively mixing layer, the mixed layer, and the pycnocline are shown in Table 3 and Figures 9 and 10. To illustrate different regimes of mixing, we refer to three example stations shown in Figure 6. The stations 54502 and 54901 (Figures 6a and 6b) show that in case of strong mixing, AMLD and MLD are nearly the same. Within the AML, the Thorpe scales range between 1 and 21 m and reveal strong mixing in the upper 100 m. K_T and K_ε are estimated as $2.96 \times 10^{-2} \pm 4.21 \times 10^{-2}$ m^2 s^{-1} and $5.80 \times 10^{-2} \pm 2.08 \times 10^{-1}$ m^2 s^{-1} (station 54502) and $5.30 \times 10^{-2} \pm 6.01 \times 10^{-2}$ m^2 s^{-1} and $2.02 \times 10^{-2} \pm 1.11 \times 10^{-1}$ m^2 s^{-1} (station 54901), respectively. The station 55101 (Figure 6c), however, shows vertical profiles of K_T and K_ε in case of restratification during noon at Julian day 69. In this example, the AMLD is defined by the depth at which the dissipation rate decreases exponentially from $>10^{-7}$ to 10^{-8} W kg^{-1} just below the lower boundary of the thin surface. At this station, the vertical averages of K_T and K_ε are $1.34 \times 10^{-2} \pm 9.63 \times 10^{-3}$ m^2 s^{-1} and $2.36 \times 10^{-2} \pm 2.77 \times 10^{-2}$ m^2 s^{-1}, respectively.

[38] While the vertical averages of K_T within the AML range between $3.20 \times 10^{-3} \pm 2.46 \times 10^{-2}$ at station 55001 and $5.65 \times 10^{-2} \pm 4.86 \times 10^{-2}$ m^2 s^{-1} at station 59108, the values for K_ε within the AML range between $1.03 \times 10^{-2} \pm 1.64 \times 10^{-2}$ (station 54455) and $4.94 \times 10^{-1} \pm 3.48 \times 10^{0}$ m^2 s^{-1} (station 59313). However, please note that the high K_ε averages and standard deviations estimated both in AML and ML, e.g., at stations 54450, 58013, and 59313, may be caused by intermittency and arithmetic averaging of logarithms; this means geometric averaging on linear scale.

[39] The overall averages for the actively mixed layer are $K_T = 2.84 \times 10^{-2} \pm 3.66 \times 10^{-2}$ m^2 s^{-1} and $K_\varepsilon = 1.27 \times 10^{-1} \pm 9.4 \times 10^{-1}$ m^2 s^{-1}. The overall means for the mixed layer are $K_T = 2.26 \times 10^{-2} \pm 3.49 \times 10^{-2}$ m^2 s^{-1} and $K_\varepsilon = 8.22 \times 10^{-2} \pm 7.43 \times 10^{-1}$ m^2 s^{-1}. These values are in good agreement to previous results in a similar study described by *Cisewski et al.* [2005]. The overall mean of K_T was $1.59 \times 10^{-2} \pm 2.77 \times 10^{-2}$ m^2 s^{-1}. However, the authors pointed out that Thorpe scale-based diffusivities, which just relied on the temperature profiles in that earlier study, are only applicable to the upper 90–120 m but not deeper, where haline gradients gain importance in affecting the vertical density distribution. In the present study, we overcome this problem by using density-based Thorpe scales. The overall mean for K_T and K_ε diminishes from the actively mixed layer to the mixed layer by 20% and 35%, respectively. Vertical diffusivities below the mixed layer appear rather invariant against changes in atmospheric forcing. The overall means for the upper pycnocline (Layer 3) are $K_T = 7.98 \times 10^{-4} \pm 1.64 \times 10^{-3}$, which confirms the results for $K_T = 7.06 \times 10^{-4} \pm 1.9 \times 10^{-3}$ from the paper by *Cisewski et al.* [2005] and $K_\varepsilon = 1.04 \times 10^{-3} \pm 1.66 \times 10^{-2}$ m^2 s^{-1}.

[40] For the vertical distribution of the KPP-derived diffusivity, we distinguished between the boundary layer (BL) and the mixed layer. While the bottom of the BL was given by the KPP-derived boundary layer depth, we applied our $\Delta\sigma_T$ criterion to the assimilated density field. The vertical averages for K_{KPP} within the BL range between $1.47 \times 10^{-3} \pm 6.33 \times 10^{-4}$ and $8.64 \times 10^{-2} \pm 5.73 \times 10^{-2}$ m^2 s^{-1}. The vertical averages for K_{KPP} within the ML range between $4.92 \times 10^{-4} \pm 7.03 \times 10^{-4}$ and $7.93 \times 10^{-2} \pm 6.01 \times 10^{-2}$ m^2 s^{-1}. The overall means for the boundary layer and the mixed layer are $K_{KPP} = 3.39 \times 10^{-2} \pm 3.63 \times 10^{-2}$ m^2 s^{-1} and $K_{KPP} = 2.35 \times 10^{-2} \pm 3.38 \times 10^{-2}$ m^2 s^{-1}, respectively. While a single KPP simulation can differ by 1–2 orders of magnitude from the estimates of K_T and K_ε, when the BLD and MLD become very shallow (station 55001), the overall means agree in terms of order of magnitude.

[41] To indicate if values of K_z in the order of 10^{-4} m^2 s^{-1} appear as a rather robust estimate of vertical diffusivity within the seasonal pycnocline, we refer to the results of a mixing study, which was also conducted within a cyclonic eddy in the Antarctic Polar Front Zone. *Cisewski et al.* [2005] estimated the vertical diffusivity K_z from two different parameterizations and compared the results with Cox number- and Thorpe scale-related diffusivities deduced from MSS measurements. The overall mean for the upper thermocline was $K_T = 7.06 \times 10^{-4} \pm 1.92 \times 10^{-3}$ m^2 s^{-1}. This result was confirmed by an independent estimate of vertical eddy diffusivity. *Croot et al.* [2005] calculated the vertical diffusivity from dissolved iron by using the second moment method for a 2 d period at the bottom of the mixed layer and obtained a value $K_T = 6.7 \times 10^{-4} \pm 0.7 \times 10^{-4}$ m^2 s^{-1}.

[42] While direct estimates of vertical eddy diffusivities are generally rare in the open Southern Ocean, K_z for diffusion across the pycnocline has been estimated on few other sites using the inert tracer sulfur hexafluoride (SF_6). During the Southern Ocean Iron Enrichment Experiment performed at 140°E, 61°S and FeCycle performed at 178.5°E, 46.5°S, the SF_6-derived K_z was estimated as 1.1×10^{-5} m^2 s^{-1} $\pm 2 \times 10^{-5}$ m^2 s^{-1} [*Law et al.*, 1998, 2003] and 6.6×10^{-5} m^2 s^{-1} $\pm 1.1 \times 10^{-5}$ m^2 s^{-1} [*Croot et al.*, 2007], respectively.

5. Conclusions

[43] This study provided the rare opportunity to investigate the mixing regime over a period of about 37 d within a mesoscale eddy at the Southern Polar Front. The combination of meteorological, hydrographic, and microstructure measurements allowed a detailed investigation of the mixing regime, a clearer differentiation between mixed layer and active mixing layer depths, and an analysis of the

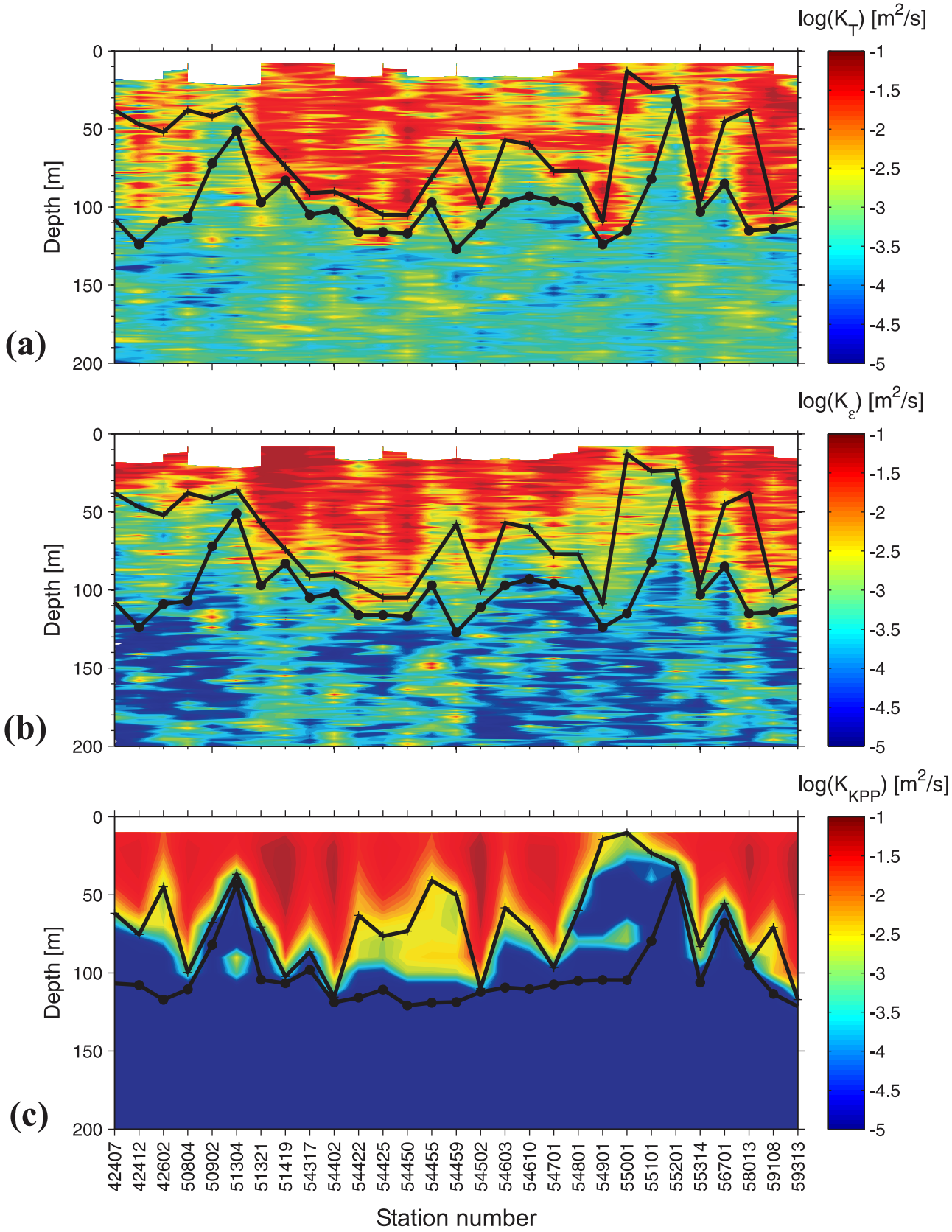

Figure 9. Vertical distribution of (a) K_T, (b) K_ε, and (c) K_{KPP} versus station number, actively mixing layer depths (black crosses), and mixed layer depths (black circles).

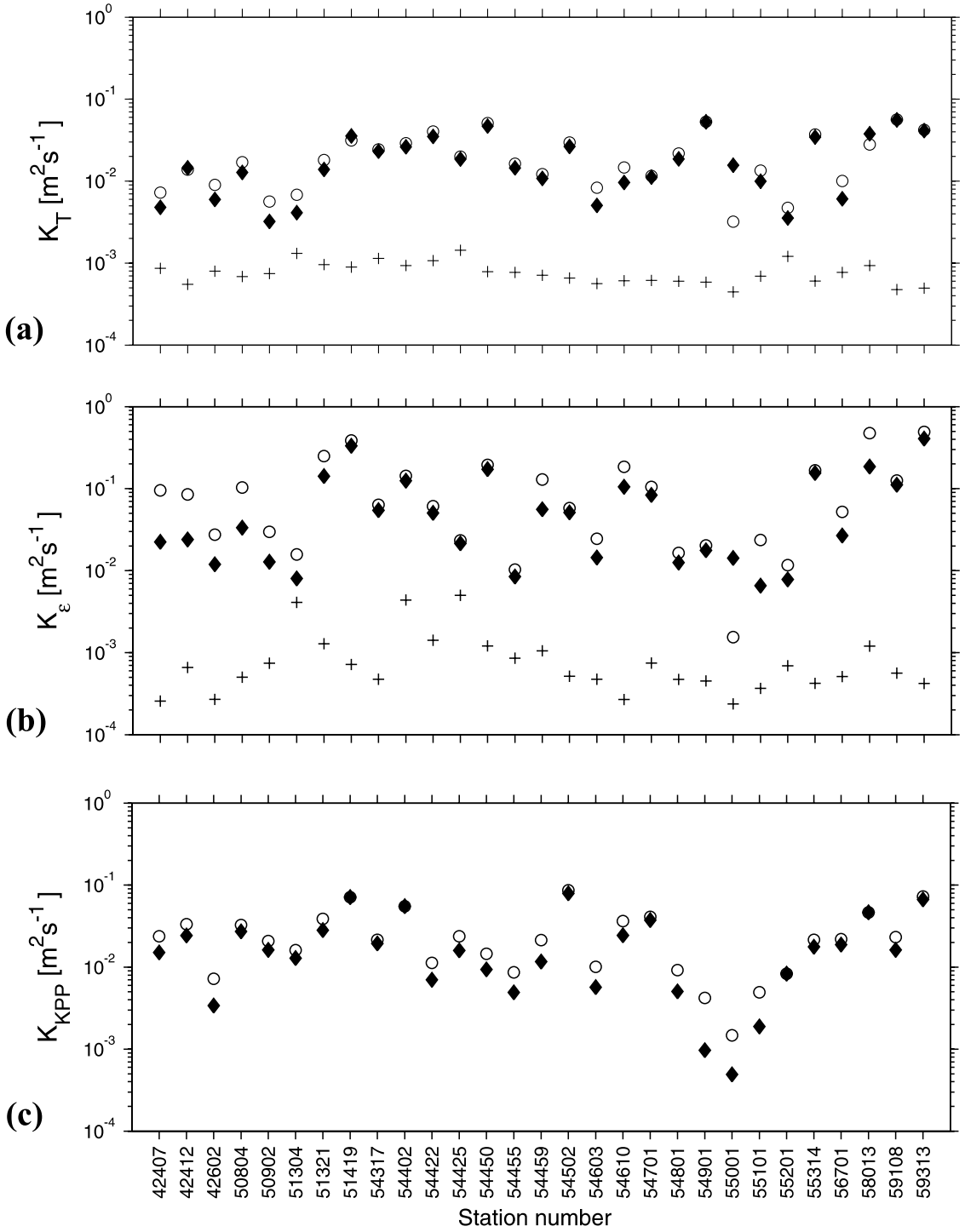

Figure 10. Vertically averaged eddy diffusivities of (a) K_T, (b) K_ε, and (c) K_{KPP} within actively mixing layer (open circles), mixed layer (black diamonds), and pycnocline (black crosses).

relationship between the mixed layer depth and the sea surface fluxes.

[44] The difference criterion of $\Delta\sigma_T$ = 0.02 kg m^{-3}, proposed by *Cisewski et al.* [2005], proved suitable to estimate the MLD. During the experiment, the mixed layer was characterized by increased Thorpe scales ranging between 2 and 21 m, which indicate strong overturning over the extent of the mixed layer at most stations. Just below the predicted mixed layer depth, the Thorpe scale decreased rapidly and showed that the observed instabilities are mainly restricted to the mixed layer. The near-surface layer reveals an exponential decrease of ε by up to 2 orders of magnitude (e.g., 10^{-5} to 10^{-7} W kg^{-1}).

[45] The mean MLD calculated from the composite of CTD- and MSS-derived data is 97.6 ± 20.6 m. In spite of a mean mixed layer of about 97.6 m, we find no significant correlation between E_{10} and MLD; the correlation coefficient varies between 0.02 and 0.22. However, the analysis

Table 3. Vertically Averaged Eddy Coefficients K_T, K_ε, and K_{KPP} Calculated for Actively Mixing Layer (Layer 1), Mixed Layer (Layer 2), and Pycnocline Layer (Layer 3)

Station	Layer 1 K, $m^2\ s^{-1}$	Layer 2 K, $m^2\ s^{-1}$	Layer 3 K, $m^2\ s^{-1}$
42407	7.25×10^{-3} ($\pm 1.31 \times 10^{-2}$)	4.78×10^{-3} ($\pm 1.20 \times 10^{-2}$)	8.65×10^{-4} ($\pm 1.64 \times 10^{-3}$)
	9.52×10^{-2} ($\pm 1.67 \times 10^{-1}$)	2.24×10^{-2} ($\pm 8.65 \times 10^{-2}$)	2.56×10^{-4} ($\pm 6.92 \times 10^{-4}$)
	2.37×10^{-2} ($\pm 1.92 \times 10^{-2}$)	1.51×10^{-2} ($\pm 1.91 \times 10^{-2}$)	
42412	1.38×10^{-2} ($\pm 1.98 \times 10^{-2}$)	1.45×10^{-2} ($\pm 2.00 \times 10^{-2}$)	5.50×10^{-4} ($\pm 7.53 \times 10^{-4}$)
	8.51×10^{-2} ($\pm 3.09 \times 10^{-1}$)	2.39×10^{-2} ($\pm 1.62 \times 10^{-1}$)	6.58×10^{-4} ($\pm 5.95 \times 10^{-3}$)
	3.34×10^{-2} ($\pm 2.53 \times 10^{-2}$)	2.43×10^{-2} ($\pm 2.63 \times 10^{-2}$)	
42602	9.00×10^{-3} ($\pm 7.32 \times 10^{-3}$)	5.96×10^{-3} ($\pm 6.79 \times 10^{-3}$)	7.97×10^{-4} ($\pm 1.69 \times 10^{-3}$)
	2.74×10^{-2} ($\pm 4.91 \times 10^{-2}$)	1.20×10^{-2} ($\pm 3.35 \times 10^{-2}$)	2.70×10^{-4} ($\pm 4.81 \times 10^{-4}$)
	7.22×10^{-3} ($\pm 5.65 \times 10^{-3}$)	3.40×10^{-3} ($\pm 4.86 \times 10^{-3}$)	
50804	1.70×10^{-2} ($\pm 1.82 \times 10^{-2}$)	1.27×10^{-2} ($\pm 1.58 \times 10^{-2}$)	6.87×10^{-4} ($\pm 1.03 \times 10^{-3}$)
	1.03×10^{-1} ($\pm 2.42 \times 10^{-1}$)	3.33×10^{-2} ($\pm 1.40 \times 10^{-1}$)	5.01×10^{-4} ($\pm 1.03 \times 10^{-3}$)
	3.27×10^{-2} ($\pm 2.29 \times 10^{-2}$)	2.72×10^{-2} ($\pm 2.43 \times 10^{-2}$)	
50902	5.64×10^{-3} ($\pm 5.70 \times 10^{-3}$)	3.22×10^{-3} ($\pm 4.58 \times 10^{-3}$)	7.45×10^{-4} ($\pm 1.33 \times 10^{-3}$)
	2.98×10^{-2} ($\pm 5.97 \times 10^{-2}$)	1.28×10^{-2} ($\pm 4.04 \times 10^{-2}$)	7.42×10^{-4} ($\pm 3.54 \times 10^{-3}$)
	2.08×10^{-2} ($\pm 1.68 \times 10^{-2}$)	1.62×10^{-2} ($\pm 1.72 \times 10^{-2}$)	
51304	6.81×10^{-3} ($\pm 1.12 \times 10^{-2}$)	4.12×10^{-3} ($\pm 8.21 \times 10^{-3}$)	1.31×10^{-3} ($\pm 3.32 \times 10^{-3}$)
	1.58×10^{-2} ($\pm 3.41 \times 10^{-2}$)	8.00×10^{-3} ($\pm 2.45 \times 10^{-2}$)	4.11×10^{-3} ($\pm 5.18 \times 10^{-2}$)
	1.61×10^{-2} ($\pm 1.51 \times 10^{-2}$)	1.29×10^{-2} ($\pm 1.49 \times 10^{-2}$)	
51321	1.80×10^{-2} ($\pm 9.66 \times 10^{-3}$)	1.39×10^{-2} ($\pm 9.96 \times 10^{-3}$)	9.59×10^{-4} ($\pm 1.05 \times 10^{-3}$)
	2.55×10^{-1} ($\pm 3.50 \times 10^{-1}$)	1.42×10^{-1} ($\pm 2.85 \times 10^{-1}$)	1.28×10^{-3} ($\pm 2.77 \times 10^{-3}$)
	3.88×10^{-2} ($\pm 3.33 \times 10^{-2}$)	2.83×10^{-2} ($\pm 3.32 \times 10^{-2}$)	
51419	3.13×10^{-2} ($\pm 3.35 \times 10^{-2}$)	3.56×10^{-2} ($\pm 4.95 \times 10^{-2}$)	8.92×10^{-4} ($\pm 1.11 \times 10^{-3}$)
	3.86×10^{-1} ($\pm 1.17 \times 10^{0}$)	3.33×10^{-1} ($\pm 1.09 \times 10^{0}$)	7.19×10^{-4} ($\pm 4.56 \times 10^{-3}$)
	7.12×10^{-2} ($\pm 5.28 \times 10^{-2}$)	7.12×10^{-2} ($\pm 5.28 \times 10^{-2}$)	
54317	2.43×10^{-2} ($\pm 2.22 \times 10^{-2}$)	2.31×10^{-2} ($\pm 2.23 \times 10^{-2}$)	1.14×10^{-3} ($\pm 1.13 \times 10^{-3}$)
	6.34×10^{-2} ($\pm 1.52 \times 10^{-1}$)	5.46×10^{-2} ($\pm 1.42 \times 10^{-1}$)	4.74×10^{-4} ($\pm 2.97 \times 10^{-3}$)
	2.16×10^{-2} ($\pm 1.77 \times 10^{-2}$)	1.94×10^{-2} ($\pm 1.80 \times 10^{-2}$)	
54402	2.90×10^{-2} ($\pm 2.61 \times 10^{-2}$)	2.61×10^{-2} ($\pm 2.56 \times 10^{-2}$)	9.34×10^{-4} ($\pm 8.87 \times 10^{-4}$)
	1.43×10^{-1} ($\pm 4.15 \times 10^{-1}$)	1.25×10^{-1} ($\pm 3.90 \times 10^{-1}$)	4.39×10^{-3} ($\pm 2.97 \times 10^{-2}$)
	5.52×10^{-2} ($\pm 4.14 \times 10^{-2}$)	5.52×10^{-2} ($\pm 4.14 \times 10^{-2}$)	
54422	4.04×10^{-2} ($\pm 3.98 \times 10^{-2}$)	3.50×10^{-2} ($\pm 3.78 \times 10^{-2}$)	1.07×10^{-3} ($\pm 1.88 \times 10^{-3}$)
	6.11×10^{-2} ($\pm 2.05 \times 10^{-1}$)	5.05×10^{-2} ($\pm 1.86 \times 10^{-1}$)	1.41×10^{-3} ($\pm 6.76 \times 10^{-3}$)
	1.13×10^{-2} ($\pm 6.46 \times 10^{-2}$)	7.00×10^{-3} ($\pm 7.16 \times 10^{-3}$)	
54425	1.99×10^{-2} ($\pm 2.16 \times 10^{-2}$)	1.85×10^{-2} ($\pm 2.11 \times 10^{-2}$)	1.44×10^{-3} ($\pm 6.42 \times 10^{-3}$)
	2.33×10^{-2} ($\pm 4.07 \times 10^{-2}$)	2.15×10^{-2} ($\pm 3.91 \times 10^{-2}$)	5.00×10^{-3} ($\pm 6.71 \times 10^{-2}$)
	2.38×10^{-2} ($\pm 1.72 \times 10^{-2}$)	1.60×10^{-2} ($\pm 1.79 \times 10^{-2}$)	
54450	5.10×10^{-2} ($\pm 5.09 \times 10^{-2}$)	4.68×10^{-2} ($\pm 4.94 \times 10^{-2}$)	7.88×10^{-4} ($\pm 7.03 \times 10^{-4}$)
	1.95×10^{-1} ($\pm 1.02 \times 10^{0}$)	1.73×10^{-1} ($\pm 9.63 \times 10^{-1}$)	1.21×10^{-3} ($\pm 4.11 \times 10^{-3}$)
	1.45×10^{-2} ($\pm 1.04 \times 10^{-2}$)	9.37×10^{-3} ($\pm 1.05 \times 10^{-2}$)	
54455	1.63×10^{-2} ($\pm 1.46 \times 10^{-2}$)	1.45×10^{-2} ($\pm 1.42 \times 10^{-2}$)	7.69×10^{-4} ($\pm 6.83 \times 10^{-4}$)
	1.03×10^{-2} ($\pm 1.64 \times 10^{-2}$)	8.46×10^{-3} ($\pm 1.51 \times 10^{-2}$)	8.54×10^{-4} ($\pm 4.03 \times 10^{-3}$)
	8.64×10^{-3} ($\pm 5.60 \times 10^{-3}$)	4.92×10^{-3} ($\pm 4.88 \times 10^{-3}$)	
54459	1.22×10^{-2} ($\pm 8.33 \times 10^{-3}$)	1.08×10^{-2} ($\pm 1.03 \times 10^{-2}$)	7.10×10^{-4} ($\pm 7.00 \times 10^{-4}$)
	1.29×10^{-1} ($\pm 2.91 \times 10^{-1}$)	5.58×10^{-2} ($\pm 1.98 \times 10^{-1}$)	1.05×10^{-3} ($\pm 3.36 \times 10^{-3}$)
	2.14×10^{-2} ($\pm 1.87 \times 10^{-2}$)	1.17×10^{-2} ($\pm 1.63 \times 10^{-2}$)	
54502	2.96×10^{-2} ($\pm 4.21 \times 10^{-2}$)	2.64×10^{-2} ($\pm 4.05 \times 10^{-2}$)	6.57×10^{-4} ($\pm 8.86 \times 10^{-4}$)
	5.80×10^{-2} ($\pm 2.08 \times 10^{-1}$)	5.13×10^{-2} ($\pm 1.96 \times 10^{-1}$)	5.16×10^{-4} ($\pm 1.16 \times 10^{-3}$)
	8.64×10^{-2} ($\pm 5.73 \times 10^{-2}$)	7.93×10^{-2} ($\pm 6.01 \times 10^{-2}$)	
54603	8.29×10^{-3} ($\pm 6.82 \times 10^{-3}$)	5.04×10^{-3} ($\pm 5.96 \times 10^{-3}$)	5.62×10^{-4} ($\pm 7.40 \times 10^{-4}$)
	2.45×10^{-2} ($\pm 4.65 \times 10^{-2}$)	1.44×10^{-2} ($\pm 3.50 \times 10^{-2}$)	4.74×10^{-4} ($\pm 1.97 \times 10^{-3}$)
	1.01×10^{-2} ($\pm 5.50 \times 10^{-3}$)	5.70×10^{-3} ($\pm 6.41 \times 10^{-3}$)	
54610	1.47×10^{-2} ($\pm 1.52 \times 10^{-2}$)	9.60×10^{-3} ($\pm 1.31 \times 10^{-2}$)	6.09×10^{-4} ($\pm 4.96 \times 10^{-4}$)
	1.85×10^{-1} ($\pm 7.57 \times 10^{-1}$)	1.05×10^{-1} ($\pm 5.74 \times 10^{-1}$)	2.68×10^{-4} ($\pm 6.08 \times 10^{-4}$)
	3.65×10^{-2} ($\pm 2.77 \times 10^{-2}$)	2.44×10^{-2} ($\pm 2.85 \times 10^{-2}$)	
54701	1.16×10^{-2} ($\pm 1.76 \times 10^{-2}$)	1.12×10^{-2} ($\pm 1.78 \times 10^{-2}$)	6.16×10^{-4} ($\pm 5.95 \times 10^{-4}$)
	1.05×10^{-1} ($\pm 2.50 \times 10^{-1}$)	8.36×10^{-2} ($\pm 2.23 \times 10^{-1}$)	7.47×10^{-4} ($\pm 4.98 \times 10^{-3}$)
	7.12×10^{-2} ($\pm 5.28 \times 10^{-2}$)	3.73×10^{-2} ($\pm 3.02 \times 10^{-2}$)	
54801	2.18×10^{-2} ($\pm 3.33 \times 10^{-2}$)	1.87×10^{-2} ($\pm 3.57 \times 10^{-2}$)	6.02×10^{-4} ($\pm 5.85 \times 10^{-4}$)
	1.65×10^{-2} ($\pm 2.43 \times 10^{-2}$)	1.25×10^{-2} ($\pm 2.21 \times 10^{-2}$)	4.71×10^{-4} ($\pm 1.36 \times 10^{-3}$)
	9.19×10^{-3} ($\pm 7.69 \times 10^{-3}$)	5.05×10^{-3} ($\pm 7.23 \times 10^{-3}$)	
54901	5.30×10^{-2} ($\pm 6.01 \times 10^{-2}$)	5.27×10^{-2} ($\pm 6.14 \times 10^{-2}$)	5.86×10^{-4} ($\pm 4.48 \times 10^{-4}$)
	2.02×10^{-2} ($\pm 1.11 \times 10^{-1}$)	1.77×10^{-2} ($\pm 1.03 \times 10^{-1}$)	4.51×10^{-4} ($\pm 1.33 \times 10^{-3}$)
	4.21×10^{-3} ($\pm 6.36 \times 10^{-4}$)	9.70×10^{-4} ($\pm 1.69 \times 10^{-3}$)	
55001	3.20×10^{-3} ($\pm 2.46 \times 10^{-2}$)	1.56×10^{-2} ($\pm 2.45 \times 10^{-2}$)	4.46×10^{-4} ($\pm 2.60 \times 10^{-4}$)
	1.54×10^{-3} ($\pm 9.22 \times 10^{-2}$)	1.42×10^{-2} ($\pm 9.13 \times 10^{-2}$)	2.37×10^{-4} ($\pm 7.04 \times 10^{-4}$)
	1.47×10^{-3} ($\pm 6.33 \times 10^{-4}$)	4.92×10^{-4} ($\pm 7.03 \times 10^{-4}$)	
55101	1.34×10^{-2} ($\pm 9.63 \times 10^{-3}$)	9.98×10^{-3} ($\pm 1.36 \times 10^{-2}$)	6.92×10^{-4} ($\pm 8.03 \times 10^{-4}$)
	2.36×10^{-2} ($\pm 2.77 \times 10^{-2}$)	6.56×10^{-3} ($\pm 1.56 \times 10^{-2}$)	3.66×10^{-4} ($\pm 1.17 \times 10^{-3}$)
	4.94×10^{-3} ($\pm 5.96 \times 10^{-3}$)	1.88×10^{-3} ($\pm 4.07 \times 10^{-3}$)	
55201	4.72×10^{-3} ($\pm 4.79 \times 10^{-3}$)	3.55×10^{-3} ($\pm 4.12 \times 10^{-3}$)	1.21×10^{-3} ($\pm 1.36 \times 10^{-3}$)
	1.17×10^{-2} ($\pm 1.19 \times 10^{-2}$)	7.80×10^{-3} ($\pm 1.07 \times 10^{-2}$)	6.91×10^{-4} ($\pm 2.30 \times 10^{-3}$)
	8.29×10^{-3} ($\pm 1.02 \times 10^{-2}$)	8.29×10^{-3} ($\pm 1.02 \times 10^{-2}$)	

Table 3. (continued)

Station	Layer 1 K, $m^2\ s^{-1}$	Layer 2 K, $m^2\ s^{-1}$	Layer 3 K, $m^2\ s^{-1}$
55314	3.71×10^{-2} ($\pm 3.33 \times 10^{-2}$)	3.44×10^{-2} ($\pm 3.35 \times 10^{-2}$)	6.05×10^{-4} ($\pm 4.93 \times 10^{-4}$)
	1.67×10^{-1} ($\pm 5.03 \times 10^{-1}$)	1.55×10^{-1} ($\pm 4.86 \times 10^{-1}$)	4.22×10^{-4} ($\pm 1.22 \times 10^{-3}$)
	2.16×10^{-2} ($\pm 1.47 \times 10^{-2}$)	1.76×10^{-2} ($\pm 1.58 \times 10^{-2}$)	
56701	1.00×10^{-2} ($\pm 8.58 \times 10^{-3}$)	6.09×10^{-3} ($\pm 7.24 \times 10^{-3}$)	7.69×10^{-4} ($\pm 7.84 \times 10^{-4}$)
	5.22×10^{-2} ($\pm 1.38 \times 10^{-1}$)	2.68×10^{-2} ($\pm 9.80 \times 10^{-2}$)	5.11×10^{-4} ($\pm 1.36 \times 10^{-3}$)
	2.19×10^{-2} ($\pm 1.90 \times 10^{-2}$)	1.88×10^{-2} ($\pm 1.92 \times 10^{-2}$)	
58013	2.79×10^{-2} ($\pm 2.62 \times 10^{-2}$)	3.77×10^{-2} ($\pm 4.04 \times 10^{-2}$)	9.35×10^{-4} ($\pm 1.40 \times 10^{-3}$)
	4.75×10^{-1} ($\pm 1.88 \times 10^{0}$)	1.85×10^{-1} ($\pm 1.05 \times 10^{0}$)	1.20×10^{-3} ($\pm 4.37 \times 10^{-3}$)
	4.64×10^{-2} ($\pm 3.67 \times 10^{-2}$)	4.64×10^{-2} ($\pm 3.67 \times 10^{-2}$)	
59108	5.65×10^{-2} ($\pm 4.86 \times 10^{-2}$)	5.56×10^{-2} ($\pm 4.99 \times 10^{-2}$)	4.76×10^{-4} ($\pm 3.71 \times 10^{-4}$)
	1.25×10^{-1} ($\pm 8.60 \times 10^{-1}$)	1.11×10^{-1} ($\pm 8.11 \times 10^{-1}$)	5.63×10^{-4} ($\pm 2.55 \times 10^{-3}$)
	2.32×10^{-2} ($\pm 1.71 \times 10^{-2}$)	1.62×10^{-2} ($\pm 1.72 \times 10^{-2}$)	
59313	4.22×10^{-2} ($\pm 4.64 \times 10^{-2}$)	4.11×10^{-2} ($\pm 5.57 \times 10^{-2}$)	4.96×10^{-4} ($\pm 5.62 \times 10^{-4}$)
	4.94×10^{-1} ($\pm 3.48 \times 10^{0}$)	4.08×10^{-1} ($\pm 3.15 \times 10^{0}$)	4.20×10^{-4} ($\pm 1.40 \times 10^{-3}$)
	7.24×10^{-2} ($\pm 5.00 \times 10^{-2}$)	6.68×10^{-2} ($\pm 5.19 \times 10^{-2}$)	
Overall means	2.84×10^{-2} ($\pm 3.66 \times 10^{-2}$)	2.26×10^{-2} ($\pm 3.49 \times 10^{-2}$)	7.98×10^{-4} ($\pm 1.64 \times 10^{-3}$)
	1.27×10^{-1} ($\pm 9.40 \times 10^{-1}$)	8.22×10^{-2} ($\pm 7.43 \times 10^{-1}$)	1.04×10^{-3} ($\pm 1.66 \times 10^{-2}$)
	3.39×10^{-2}($\pm 3.63 \times 10^{-2}$)	2.35×10^{-2}($\pm 3.38 \times 10^{-2}$)	

reveals a negative correlation between the surface buoyancy flux and the mixed layer depth. This correlation reflects the approximately diurnal forcing by the buoyancy flux. The highest correlation is -0.25 and -0.28 at time lags Δt = 13 h and Δt = 38 h, respectively.

[46] Microstructure sonde-deduced Thorpe scales and dissipation rates were used to determine the depth of the actively mixed layer. These parameters supplemented the hydrographic profiles and are necessary to discriminate actively mixing and fossil layers. Since determination of the AMLD by combination of different criteria is somewhat subjective, we also used the results of a GCM with the KPP mixed layer model. Although the obtained mixing depths of both $AMLD_{MSS}$ = 66.4 ± 28.8 m and BLD_{KPP} = 69.1 ± 29.5 m are nearly the same, several individual values differed by up to 83 m, resulting in a correlation coefficient of 0.48.

[47] The overall means of vertical diffusivities for the actively mixed layer are $K_T = 2.84 \times 10^{-2} \pm 3.66 \times 10^{-2}$ $m^2\ s^{-1}$ and $K_\varepsilon = 1.27 \times 10^{-1} \pm 9.4 \times 10^{-1}$ $m^2\ s^{-1}$. The values diminished from the actively mixed layer to the mixed layer by 20% and 35%. Eddy diffusivities in the pycnocline below the mixed layer appear rather invariant against changes in atmospheric forcing. The overall mean for the upper thermocline (layer 4) are $K_T = 7.98 \times 10^{-4} \pm 1.64 \times 10^{-3}$ $m^2\ s^{-1}$ and $K_\varepsilon = 1.04 \times 10^{-3} \pm 1.66 \times 10^{-2}$ $m^2\ s^{-1}$, which corroborates the results for $K_T = 7.06 \times 10^{-4} \pm 1.9 \times 10^{-3}$ $m^2\ s^{-1}$ from work by *Cisewski et al.* [2005].

[48] **Acknowledgments.** This work was part of the iron fertilization experiment EIFEX (*Polarstern* cruise ANT XXI/3), which was successfully conducted under the leadership of the chief scientist Victor Smetacek. Santiago Gonzales, Harry Leach, Harald Rohr, and Klaus Loquay contributed substantially to the collection of the comprehensive hydrographic and microstructure data sets; Harry Leach also provided the optimal interpolation routines for calculating the stream function. We gratefully acknowledge the support provided by the captain, officers, and crew of the R/V *Polarstern*.

References

Blanke, B., S. Speich, G. Madec, and R. Mauge (2002), A global diagnostic of interior ocean ventilation, *Geophys. Res. Lett.*, *29*(8), 1267, doi:10.1029/2001GL013727.

Brainerd, K. E., and M. C. Gregg (1995), Surface mixed and mixing layer depths, *Deep Sea Res., Part I*, *42*, 1521–1543, doi:10.1016/0967-0637(95)00068-H.

Cisewski, B., V. H. Strass, and H. Prandke (2005), Upper-ocean vertical mixing in the Antarctic Polar Front Zone, *Deep Sea Res., Part II*, *52*, 1087–1108, doi:10.1016/j.dsr2.2005.01.010.

Croot, P. L., et al. (2005), Spatial and temporal distribution of Fe (II) and H_2O_2 during EisenEx, an open ocean mesoscale iron enrichment, *Mar. Chem.*, *95*, 65–88, doi:10.1016/j.marchem.2004.06.041.

Croot, P. L., R. D. Frew, S. Sander, K. A. Hunter, M. J. Ellwood, S. E. Pickmere, E. R. Abraham, C. S. Law, M. J. Smith, and P. W. Boyd (2007), Physical mixing effects on iron biogeochemical cycling: FeCycle experiment, *J. Geophys. Res.*, *112*, C06015, doi:10.1029/2006JC003748.

Dillon, T. M. (1982), Vertical overturns: A comparison of Thorpe and Ozmidov length scales, *J. Geophys. Res.*, *87*(C12), 9601–9613, doi:10.1029/JC087iC12p09601.

Fairall, C. W., E. F. Bradley, J. E. Hare, A. A. Grachev, and J. B. Edson (2003), Bulk parameterization of air-sea fluxes: Updates and verification for the COARE algorithm, *J. Clim.*, *16*, 571–591, doi:10.1175/1520-0442(2003)016<0571:BPOASF>2.0.CO;2.

Firing, E. (1991), Acoustic Doppler current profiling measurements and navigation, in *WOCE Hydrographic Program Office Report WHPO 91–9*, *WOCE Rep. 68/91*, 24 pp., World Ocean Circ. Exp., Woods Hole, Mass.

Francois, R., M. A. Altabet, E.-F. Yu, D. M. Sigman, M. P. Bacon, M. Frank, G. Bohrmann, G. Bareille, and L. D. Labeyrie (1997), Contribution of Southern Ocean surface-water stratification to low atmospheric CO_2 concentrations during the last glacial period, *Nature*, *389*, 929–935, doi:10.1038/40073.

Kara, A. B., P. A. Rochford, and H. E. Hurlburt (2000), An optimal definition for ocean mixed layer depth, *J. Geophys. Res.*, *105*(C7), 16,803–16,821, doi:10.1029/2000JC900072.

König-Langlo, G., B. Loose, and B. Bräuer (2006), 25 years of *Polarstern* meteorology (1982–2006), *WDC-MARE Rep. 0004 (2006)*, 144 pp., Alfred Wegener Inst. for Polar and Mar. Res., Bremerhaven, Germany.

Large, W. G., and S. Pond (1981), Open ocean momentum flux measurements in moderate to strong winds, *J. Phys. Oceanogr.*, *11*, 324–336, doi:10.1175/1520-0485(1981)011<0324:OOMFMI>2.0.CO;2.

Large, W. G., and S. Pond (1982), Sensible and latent heat flux measurements over the ocean, *J. Phys. Oceanogr.*, *12*, 464–482, doi:10.1175/1520-0485(1982)012<0464:SALHFM>2.0.CO;2.

Large, W. G., J. C. McWilliams, and S. C. Doney (1994), Oceanic vertical mixing: A review and a model with a nonlocal boundary layer parameterization, *Rev. Geophys.*, *32*(4), 363–403, doi:10.1029/94RG01872.

Law, C. S., A. J. Watson, M. I. Liddicoat, and T. Stanton (1998), Sulphur hexafluoride as a tracer of biogeochemical and physical processes in an open-ocean iron fertilisation experiment, *Deep Sea Res., Part II*, *45*, 977–994, doi:10.1016/S0967-0645(98)00022-8.

Law, C. S., E. R. Abraham, A. J. Watson, and M. I. Liddicoat (2003), Vertical eddy diffusion and nutrient supply to the surface mixed layer of the Antarctic Circumpolar Current, *J. Geophys. Res.*, *108*(C8), 3272, doi:10.1029/2002JC001604.

Levitus, S., and T. P. Boyer (1994), *Temperature*, vol. 4, *World Ocean Atlas 1994*, *NOAA Atlas Natl. Environ. Satell. Data and Inf. Serv.*, vol. 4, 117 pp., U.S. Gov. Print. Off., Washington, D.C.

Levitus, S., R. Burgett, and T. P. Boyer (1994), *Salinity*, vol. 3, *World Ocean Atlas 1994*, *NOAA Atlas Natl. Environ. Satell. Data and Inf. Serv.*, vol. 3, 99 pp., U.S. Gov. Print. Off., Washington, D.C.

Lorbacher, K., D. Dommenget, P. P. Niiler, and A. Koehl (2006), Ocean mixed layer depth: A subsurface proxy of ocean-atmosphere variability, *J. Geophys. Res.*, *111*, C07010, doi:10.1029/2003JC002157.

Losch, M., R. Schukay, V. Strass, and B. Cisewski (2006), Comparison of a NLOM data assimilation product to direct measurements in the Antarctic Polar Frontal Zone: A case study, *Ann. Geophys.*, *24*(1), 3–6.

Lozovatsky, I., M. Figueroa, E. Roget, H. J. S. Fernando, and S. Shapovalov (2005), Observation and scaling of the upper mixed layer in the North Atlantic, *J. Geophys. Res.*, *110*, C05013, doi:10.1029/2004JC002708.

Lozovatsky, I., E. Roget, H. J. S. Fernando, M. Figueroa, and S. Shapovalov (2006), Sheared turbulence in a weakly stratified ocean, *Deep Sea Res., Part I*, *53*, 387–407, doi:10.1016/j.dsr.2005.10.002.

Lukas, R., and E. Lindstrom (1991), The mixed layer of the western equatorial Pacific Ocean, *J. Geophys. Res.*, *96*, suppl., 3343–3357.

Luyten, J. R., J. Pedlovsky, and H. Stommel (1983), The ventilated thermocline, *J. Phys. Oceanogr.*, *13*, 292–309, doi:10.1175/1520-0485(1983)013<0292:TVT>2.0.CO;2.

Moum, J. N., and W. D. Smyth (2001), Upper ocean mixing processes, in *Encyclopedia of Ocean Sciences*, vol.6, edited by J. H. Steele, K. K. Turekina, and S. A. Thorpe, pp. 3093–3100, Elsevier, New York.

Osborn, T. R. (1980), Estimates of the local rate of vertical diffusion from dissipation measurements, *J. Phys. Oceanogr.*, *10*, 83–89, doi:10.1175/1520-0485(1980)010<0083:EOTLRO>2.0.CO;2.

Ozmidov, R. V. (1965), On the turbulent exchange in a stably stratified ocean, *Atmos. Oceanic Phys.*, *8*, 853–860.

Prandke, H., K. Holtsch, and A. Stips (2000), MITEC technology development: The microstructure/turbulence measuring system MSS, *Tech. Rep. EUR 19733 EN*, 75 pp., Eur. Comm., Ispra, Italy.

Shay, T. J., and M. C. Gregg (1986), Convectively driven turbulent mixing in the upper ocean, *J. Phys. Oceanogr.*, *16*, 1777–1798, doi:10.1175/1520-0485(1986)016<1777:CDTMIT>2.0.CO;2.

Siedler, G., and H. Peters (1986), Properties of sea water, in *Oceanography*, edited by J. Sündermann, pp. 233–264, Springer, New York.

Smetacek, V. (2005), Fahrtabschnitt ANTXXI/3 Kapstadt-Kapstadt, *Rep. Polar Mar. Res.*, *500*, 3–135.

Sprintall, J., and D. Roemmich (1999), Characterizing the structure of the surface layer in the Pacific Ocean, *J. Geophys. Res.*, *104*(C10), 23,297–23,311, doi:10.1029/1999JC900179.

Strass, V. H., and E.-M. Nöthig (1996), Seasonal shifts in ice edge phytoplankton blooms in the Barents Sea related to the water column stability, *Polar Biol.*, *16*, 409–422, doi:10.1007/BF02390423.

Strass, V. H., H. Leach, and J. D. Woods (1992), On the seasonal development of mesoscale variability: The influence of the seasonal pycnocline formation, *Deep Sea Res., Part A*, *39*, 1627–1639, doi:10.1016/0198-0149(92)90052-U.

Strass, V. H., A. C. Naveira Garabato, R. T. Pollard, H. I. Fischer, I. Hense, J. T. Allen, J. F. Read, H. Leach, and V. Smetacek (2002), Mesoscale frontal dynamics: Shaping the environment of primary production in Antarctic Circumpolar Current, *Deep Sea Res., Part II*, *49*, 3735–3769, doi:10.1016/S0967-0645(02)00109-1.

Sverdrup, H. U. (1953), On conditions for the vernal blooming of phytoplankton, *J. Cons. Cons. Int. Explor. Mer*, *18*, 287–295.

Thorpe, S. A. (1977), Turbulence and mixing in a Scottish loch, *Philos. Trans. R. Soc. London, Ser. A*, *286*, 125–181, doi:10.1098/rsta.1977.0112.

Tranter, D. J. (1982), Interlinking of physical and biological processes in the Antarctic Ocean, *Oceanogr. Mar. Biol.*, *20*, 11–35.

Troen, I. B., and L. Mahrt (1986), A simple model of the atmospheric boundary layer; sensitivity to surface evaporation, *Boundary Layer Meteorol.*, *37*, 129–148, doi:10.1007/BF00122760.

Woods, J. D. (1985), The physics of thermocline ventilation, in *Coupled Ocean-Atmosphere Models*, edited by J. C. J. Nihoul, pp. 543–590, Elsevier, Amsterdam.

Wunsch, C. (1998), The work done by the wind on the oceanic general circulation, *J. Phys. Oceanogr.*, *28*, 2332–2340, doi:10.1175/1520-0485(1998)028<2332:TWDBTW>2.0.CO;2.

Zawada, D. G., R. V. Zaneveld, E. Boss, W. D. Gardner, M. J. Richardson, and A. V. Mishonov (2005), A comparison of hydrographically and optically mixed layer depths, *J. Geophys. Res.*, *110*, C11001, doi:10.1029/2004JC002417.

B. Cisewski, Institut für Umweltphysik, Abteilung Ozeanographie, Universität Bremen, P.O. Box 330440, D-28334 Bremen, Germany. (boris.cisewski@awi.de)

M. Losch and V. H. Strass, Alfred Wegener Institut für Polar und Meeresforschung, P.O. Box 120161, D-27515 Bremerhaven, Germany.

H. Prandke, ISW-Wassermesstechnik, Lenzer Strasse 5, D-17213 Petersdorf, Germany.